Bioactive Materials 13 (2022) 64–81

Contents lists available at ScienceDirect

Bioactive Materials

journal homepage: www.keaipublishing.com/en/journals/bioactive-materials

Oxygen generating scaffolds regenerate critical size bone defects

Sanika Suvarnapathaki [a,b], Xinchen Wu [a,b], Tengfei Zhang [c], Michelle A. Nguyen [b], Anastasia A. Goulopoulos [b], Bin Wu [c], Gulden Camci-Unal [b,d,*]

[a] Biomedical Engineering and Biotechnology Program, University of Massachusetts Lowell, One University Avenue, Lowell, MA, 01854, USA
[b] Department of Chemical Engineering, University of Massachusetts Lowell, One University Avenue, Lowell, MA, 01854, USA
[c] Department of Neurosurgery, Sanbo Brain Hospital, Capital Medicine University, Beijing, 100069, China
[d] Department of Surgery, University of Massachusetts Medical School, 55 Lake Avenue North, Worcester, MA, 01605, USA

ARTICLE INFO

Keywords:
Bone
Cranial regeneration
Critical size defect
Oxygen
Calcium peroxide

ABSTRACT

Recent innovations in bone tissue engineering have introduced biomaterials that generate oxygen to substitute vasculature. This strategy provides the immediate oxygen required for tissue viability and graft maturation. Here we demonstrate a novel oxygen-generating tissue scaffold with predictable oxygen release kinetics and modular material properties. These hydrogel scaffolds were reinforced with microparticles comprised of emulsified calcium peroxide (CaO_2) within polycaprolactone (PCL). The alterations of the assembled materials produced constructs within 5 ± 0.81 kPa to 34 ± 0.9 kPa in mechanical strength. The mass swelling ratios varied between 11% and 25%. Our *in vitro* and *in vivo* results revealed consistent tissue viability, metabolic activity, and osteogenic differentiation over two weeks. The optimized *in vitro* cell culture system remained stable at pH 8–9. The *in vivo* rodent models demonstrated that these scaffolds support a 70 mm^3 bone volume that was comparable to the native bone and yielded over 90% regeneration in critical size cranial defects. Furthermore, the *in vivo* bone remodeling and vascularization results were validated by tartrate-resistant acid phosphatase (TRAP) and vascular endothelial growth factor (VEGF) staining. The promising results of this work are translatable to a repertoire of regenerative medicine applications including advancement and expansion of bone substitutes and disease models.

1. Introduction

According to the National Institutes of Health (NIH), there are 1.9 million cases projected annually of patients who will acquire cranial fractures [1]. Among these common cases are pediatric patients who constitute a broad range of 2%–20% of the pediatric head trauma cases that will lead to cranial fractures [2]. These critical orthopedic defects are clinically remedied through bone autografts and allografts [3]. Regardless, the clinical discrepancy continues between the number of patients who suffered a critical bone injury and availability of these tissue graft for patients. The field of bone tissue engineering is motivated to expand the options for bone substitutes, as well as advance the state-of-the-art techniques that support osteogenesis and bone remodeling. Importantly, the research in this therapeutic area aims to preserve the myriad of intrinsic functions found natively in bone after physical trauma. Bone mechanically supports and protects internal organs and tissues while also providing storage units for inorganic minerals, such as calcium. The complex and organized structure of bone is essential for vital physiological processes such as hematopoiesis [3]. Therefore, the research efforts to establish mechanically competent biomaterials with osteoconductive and osteoinductive behaviors that mimic these features in bone have been increasingly sought.

As of 2021, there has been an estimated $2.78 billion global market for bone remodeling biomaterials, such as bone grafts and other synthetic substitutes [4]. Despite immense progress, autografts remain as the gold standard for bone substitutes due to their superior osteoinductive and osteoconductive properties, and low immunogenicity. The caveats of using bone allografts include their limited availability and the clinical risks, including donor site morbidity post-surgery. Alternatively, bone allografts have partially addressed clinical accessibility, but still harbor possible risks such as disease transmission and immunological rejection [5]. Recent reviews on the gold standard have shown both the

Peer review under responsibility of KeAi Communications Co., Ltd.
* Corresponding author. Department of Chemical Engineering, University of Massachusetts Lowell, One University Avenue, Lowell, MA, 01854, USA.
E-mail address: Gulden_CamciUnal@uml.edu (G. Camci-Unal).

https://doi.org/10.1016/j.bioactmat.2021.11.002
Received 2 August 2021; Received in revised form 30 September 2021; Accepted 1 November 2021
Available online 10 November 2021

tremendous clinical need and the opportunities to expand and commercialize bone substitutes for access to patients [3,6]. In particular, this market has been forecasted to reach $3.3 billion across 49 international markets by 2023 [7]. The achievement of clinically translatable bone substitutes, however, requires robust and well-characterized biocompatible materials for clinical approval.

Biomaterial selection for bone substitutes is critical to support both biomimetic properties and application in the clinical setting [8]. Materials such as calcium phosphate cement and hydroxyapatite are extensively employed in treating and repairing craniofacial defects. Specifically, calcium phosphate has been preferred for its injectability as a material, and its ability to promote vascularization during osteogenesis [9–11]. Hydroxyapatite is a native mineral found in human bone and has been integrated in fillings for significantly biomimetic and bioactive bone substitutes [12,13]. Hydroxyapatite also provides the mechanical strength required to direct bone regeneration but has limited capacity to continue this support at late stages of tissue remodeling [12,14]. These biomaterials in combination with other biological factors have been heavily investigated to emulate the native bone microenvironment and to increase scaffold effectiveness [15–17]. The other biological factors are related to the integration of the bone substitute into the host system.

Various growth factors have been utilized to bioengineer scaffolds for *in vitro* and *in vivo* applications. Bone morphogenic proteins (BMPs) are commonly included to directly induce osteogenesis, while other factors such as vascular endothelial growth factor (VEGF) promote neovascularization during bone remodeling [18,19]. The limitation of these approaches is that they require neovascularization to continue until vascular maturation is achieved [20]. The vascularization process supports osteogenesis by providing a network to deliver essential growth factors, nutrients, and oxygen for cell viability and metabolic processes [21]. The absence of sufficient vascularization in the first 4–6 weeks of bone remodeling presents a significant reduction in oxygen availability. This long-term oxygen insufficiency risks hypoxia-induced necrosis in the tissue site [15]. Oxygen has been shown to accelerate wound healing and maintain tissue viability during this period. For instance, in clinical practice, hyperbaric therapy is often used to treat wound injury sites by supplying oxygen to a targeted area under a specified pressure [21–26]. Beyond therapeutic benefit, oxygen delivery has become a central component in bone scaffold viability and function. Therefore, addressing this lack of oxygen supply in artificial bone constructs has potential to support robust bone regeneration and bone remodeling *in vitro* and *in vivo*.

Oxygen-generating biomaterials (OGM) can robustly capture these biomimetic characteristics and environmental conditions for bone regeneration. This recent class of tissue scaffolds are self-sustaining until homogeneous vascularization is achieved. These biomaterials also possess porosity and bioactive components that establish conducive microenvironments for osteogenesis [21,27]. Furthermore, oxygen-generating scaffolds function to support osteogenesis by providing continuous oxygen as they integrate into the injury site via oxygen carriers [21,28]. Often, the oxygen carriers, such as solid peroxides, liquid peroxides, or fluorocarbons, are deposited within the material matrix. Among these materials, solid calcium peroxide has been shown to release the highest concentration of oxygen in aqueous environments [21,29]. Upon interaction with water from the surrounding tissue microenvironment or scaffold matrix, the compound undergoes hydrolytic degradation which results in the release of oxygen as a product.

The fundamental concern associated with using solid peroxides in scaffolds has been the potential for rapid burst oxygen release that may further damage the surrounding tissues or cause unpredictable oxygen release kinetics [30,31]. The manipulation of the hydrolysis kinetics is a highly feasible approach to control the rates of oxygen release *in vitro* tissue culture [32]. Specifically, the introduction of a hydrophobic phases within these oxygen-generating materials is a notable strategy to reduce the contact of the solid peroxide with aqueous environment [21, 30]. Herein, we describe the integration of calcium peroxide (CaO_2) within polycaprolactone (PCL), as a hydrophobic barrier, to synthesize oxygen-generating microparticles for bone tissue constructs. These microparticles reinforced a gelatin-based hydrogel to assemble a bioactive oxygen-releasing scaffold. This paper discusses extensive *in vitro* and *in vivo* characterization of the biological, chemical, and mechanical properties of the scaffold. The interplays of these properties demonstrated exceptional effects on the cell viability, cellular functions, cranial osteogenesis, and significant regeneration in critical size calvaria defects.

2. Materials & methods

2.1. Materials

Porcine skin gelatin, methacrylic anhydride (MAA), and calcium peroxide were obtained from Sigma-Aldrich (St. Louis, MO). Polycaprolactone (PCL) was procured from Fisher Scientific. Dulbecco's phosphate buffered saline (DPBS), Dulbecco's Modified Eagle's Medium (DMEM – low glucose), fetal bovine serum (FBS), trypsin-ethylenediaminetetraacetic acid (EDTA) 0.25%, and penicillin/streptomycin (P/S) were procured from Gibco (Thermo Fisher Scientific, Waltham, MA). Alamar Blue reagent was obtained from Invitrogen (Grand Island, NY). 2-hydroxy-1-[4-(hydroxyethoxy) phenyl]-2-methyl-1propanone (Irgacure 2959) was acquired from BASF Corporation (Florham Park, NJ). Lactate Dehydrogenase (LDH) activity kit was purchased from Thermo Fisher Scientific (Waltham, MA). Caspase Glo 3/7 assay kit was procured from Promega (Madison, WI). NeoFox Oxygen sensing probe was purchased from Ocean Optics Inc (Orlando, FL). These reagents were used in the formulation as received without further purification of the products.

2.2. Synthesis of gelatin methacrylate (GelMA)

The precursor hydrogel solution was formulated with 5% (w/v) porcine GelMA and 0.5% (w/v) Irgacure 2959 photoinitiator solution. The gelatin composed of 10 g porcine skin gelatin dissolved in 100 mL DPBS under stirring conditions at 50 °C. The solubilized gelatin was combined with 8 mL of methacrylic anhydride (MAA), which was added dropwise under constant stirring at 200 rpm and 50 °C for 4 h. This process was optimized to allow the methacrylation of the gelatin backbone. The mixture was then diluted with 300 mL of DPBS to halt the reaction and was transferred into nitrocellulose membranes. The GelMA was dialyzed with distilled water for one week under constant magnetic stirring at 40 °C and 180 rpm. The modified gelatin was temporarily stored at -80 °C prior to lyophilization. The lyophilized GelMA polymer was obtained after one week in the form of a foam.

2.3. Oxygen-generating microparticle synthesis

The oxygen-generating microparticles composed of emulsified CaO_2 in PCL, which functioned as the oxygen carrier and the hydrophobic barrier, respectively. The hydrophobic phase was prepared by dissolving PCL in chloroform for a 13.5% (w/v) solution under constant magnetic stirring. In order to determine the optimum PCL concentration, a range of PCL concentrations between 5% and 20% w/v were investigated in our previous study for its oxygen release potential and kinetics in GelMA [29]. It was observed that a 13.5% w/v PCL concentration offered the most controlled and sustained oxygen release kinetics over a period of five weeks. Therefore, based on the observations from our previous study, a 13.5% w/v PCL concentration was chosen. The CaO_2 was added into the PCL at 0, 30, 60, and 90 mg/mL concentrations to generate variations of microparticles (Table 1). A 0.5% (w/v) low molecular weight PVA solution served as the aqueous phase for microparticle fabrication. The viscous phase, PCL-CaO_2, solution was added dropwise to the aqueous phase under magnetic stirring at 920 rpm to yield the

Table 1
Nomenclature for the oxygen-generating scaffolds.

Scaffold Nomenclature	GelMA (%wt/v)	PCL (w/v)	Calcium peroxide (mg/mL) in 13.5% (w/v) PCL	Calcium peroxide in GelMA (mg)
OGM_0	5	13.5	0	0
OGM_{30}	5	13.5	30	4
OGM_{60}	5	13.5	60	8
OGM_{90}	5	13.5	90	12

microparticles. These microparticles were centrifuged at 800 rpm to separate these phases. The aqueous and viscous phases were removed to isolate the pellet of microparticles. The microparticles were washed three times with hot water to avoid residual PVA. The remaining chloroform was evaporated by placing the microparticles in a vacuum desiccator for 4 h.

2.4. Oxygen-generating scaffold fabrication

The oxygen-generating scaffolds were assembled using the synthesized microparticles and GelMA. The oxygen-generating scaffolds were fabricated with the addition of 0 mg, 4.05 mg, 8.1 mg, or 12.15 mg CaO_2 per mL of GelMA within a 13.5% (w/v) PCL phase. These microparticles were resuspended in the GelMA prepolymer to reinforce polymer matrix with the oxygen-releasing component. Each scaffold possessed a volume of 40 μL GelMA prepolymer which yielded an 8 mm diameter with a 3 mm thickness upon photocrosslinking. The oxygen generating microparticles were mixed into 5% (w/v) GelMA prepolymer solution at 13.5% (w/v) concentration. Subsequently, the microparticle-GelMA mixture was pipetted to a 96-well plate. The polymer precursors were photocrosslinked simultaneously with ultraviolet (UV) light (Omnicure S2000, EXFO Photonic Solutions Inc., Ontario, Canada) at 4 mW/cm^2 for 20–130 s depending on the scaffold compositions. In addition, these scaffolds were also fabricated for mechanical characterization. The optimized UV crosslinking times for the OGM_0, OGM_{30}, OGM_{60}, and OGM_{90} scaffolds were: 20, 40, 80, and 130 s, respectively. The resulting gels were stored in DPBS for swelling, degradation, compression tests, and scanning electron microscopy (SEM) imaging.

2.5. Swelling and degradation analysis

The hydrogels were submerged in DPBS for 48 h to allow equilibrium swelling prior these analyses. These experiments were performed in quadruplicates for each scaffold composition. In the swelling analysis, the hydrogels were removed from the DPBS and excess liquid was carefully blotted. The hydrogels were then transferred to punctured microcentrifuge tubes, weighed, and stored at −80 °C overnight. These samples were subsequently lyophilized for 24 h and weighed again to obtain the dry weight of the scaffolds. The wet weights of the gels were divided by their corresponding dry weights to determine the swelling ratios. These ratios were converted into percentage values.

Similarly, the initial dry weight of the hydrogel was obtained for the degradation analysis. The dry weight of the sample was calculated by subtracting the weight of the empty container from the combined weight of the freeze-dried sample and container. The lyophilized gels were rehydrated in 1 mL of DPBS for 24 h. Following, the DPBS was replaced with 1 mL of collagenase type II in DPBS at a 2.5 U/mL concentration. The enzymatic degradation of these samples occurred on a shaker at 70 rpm in a 37 °C incubator. The remaining mass of each hydrogel was measured at time points 3, 6, 12, 18, 24, 36, and 48 h. At each time interval, the samples were washed with PBS three times to stop degradation of the material. The gels were frozen at −80 °C overnight before lyophilization to obtain the dry weights of the degraded samples. The dry weights of the samples were acquired after degradation at each time interval. The dry weight after degradation was divided by the initial weight of the hydrogel. The resulting values were converted to percentages which represent the percent mass remaining.

2.6. Mechanical analysis

This study evaluated the compressive moduli of each scaffold composition. Uniform shapes of the oxygen-generating scaffold samples were formed using an 8 mm biopsy punch after 48 h of swelling in DPBS. These compression tests were conducted with a 0.0010 N preload force at an isothermal temperature of 23 °C, soak time of 1 min, force ramp rate of 0.1 N/min, and upper force limit set to 2 N. The linear region of the stress-strain curve was used to extrapolate the compressive modulus of each scaffold condition.

2.7. Scanning electron microscopy (SEM) imaging

The porosity of oxygen-generating scaffolds was characterized through SEM imaging (JEOL 5200 SEM). The scaled hydrogel samples were flash frozen in liquid nitrogen, lyophilized, and coated with gold under an argon atmosphere. The samples were then broken and mounted on aluminum stubs with double sided carbon tape to image the scaffold cross-sections. The SEM imaging was also utilized to reveal the morphology of the PCL-CaO_2 microparticles encapsulated within the GelMA matrix.

2.8. Three-dimensional (3D) cell encapsulation in oxygen-generating scaffolds

Three-dimensional (3D) encapsulation of MC3T3-E1 preosteoblasts in the oxygen-generating scaffolds was performed. The cytocompatibility studies used a cell seeding density of 5×10^6 cells/mL. The cells were trypsinized from the cell culture flasks and centrifuged to pellet the cells. The cell count was obtained to determine the appropriate number of cells to resuspend in the scaffold prepolymer solution. As previously described, the cell-laden precursor solutions were pipetted into a 96-well plate. These cell-laden scaffolds were simultaneously UV-crosslinked. The cell-laden scaffolds were used for extensive biological assessment of the material for 14 days under hypoxia.

2.9. Measurement of oxygen release profiles

The oxygen release profiles of the scaffolds were obtained under controlled hypoxic conditions. Specifically, the oxygen concentration was kept at 2% inside the chamber (StemCell Technologies Hypoxia Chamber) to study the oxygen release kinetics from the scaffolds. Therefore, the tissue constructs were restricted to the oxygen from the microparticles. The media in the cell culture systems was supplemented with 1 mg/mL catalase. Catalase is an enzyme that is produced in the liver and is known to improve the conversion efficiency of the intermediate hydrogen peroxide to oxygen. The fluctuations in dissolved oxygen concentrations in cell culture media were recorded over a 14-day time course. This study utilized a handheld optical oxygen-sensing probe (NeoFox) to measure the amount of dissolved oxygen in the media of the cell culture systems (Fig. 2). The resulting oxygen release profiles of scaffolds were comparatively analyzed in the presence of cells and catalase.

2.10. Metabolic activity, osteogenic differentiation, cytotoxicity, apoptosis, and pH measurements

The biological performance of the tissue constructs was evaluated through cell viability, cytotoxicity, apoptosis, and osteogenic differentiation assays. These tissue constructs were cultured in DMEM medium supplemented with 10% (v/v) fetal bovine serum (FBS) and 5% (v/v) penicillin/streptomycin. The cell cultures were maintained at 37 °C with 5% carbon dioxide (CO_2), with cell culture media renewal every 2–3

days. The results of these assays have been reported as the average of quadruplicates. Specifically, functional benefits of the tissue scaffolds were evaluated in terms of metabolic activity and osteogenic differentiation. The metabolic activities of each scaffold were assessed through the Alamar Blue assay. This assay was conducted according to the manufacturer's protocol. The fluorescence values of the supernatant of the samples were read at 560nm/590 nm. The alkaline phosphatase (ALP) activity assay determined presence of an early marker of osteogenic differentiation on day 0, 1, 4, 7, 10, and 14 in *in vitro* cell culture. ALP is an enzyme specific to bone and was used a biomarker of early osteogenic differentiation. A commercial kit for ALP detection (Anaspec, Inc., Fremont, CA) in the tissue constructs was used as per the manufacturer's protocol. The absorbance results were normalized by the day 0 data.

The *in vitro* adverse effects were investigated through the lactate dehydrogenase (LDH) assay (Invitrogen) and Caspase Glo 3/7 assay (Promega). The LDH assay was performed to evaluate the cytotoxic effects of the oxygen-generating scaffolds. The released LDH catalyzes the conversion of lactate to pyruvate and reduces NAD+ to NADH in the anaerobic metabolic pathway. The product of this reaction, diaphorase, was utilized. NADH ultimately reduces a tetrazolium salt (INT) to a red formazan. In principle, the fluorescence of formazan is directly proportional to the LDH released by the cells in the culture media [33]. This assay was conducted as per the manufacturer's protocol, and the absorbance was read at a wavelength of 490 nm. The luminescence readings directly correlated to the apoptotic activities of each tissue construct. Finally, the stability of the hypoxic cell culture system was monitored for stability through changes in pH. The pH of the cell culture solution was analyzed as a potential contributing factor to viability and metabolic activity of the tissue constructs. The effect of the oxygen-generating scaffolds on the pH of the cell culture media was recorded over a 14-day *in vitro* experiment. For this analysis, commercial pH strips were used to measure the pH.

2.11. Gene expression

The RNA of the 3D-encapsulated preosteoblasts was extracted from the oxygen-generating scaffolds after day 14 of culture period using the RNAqueous Kit (Invitrogen) as per the manufacturer's protocol. A Nanodrop2000 system was used to quantify the RNA. Then, RT-qPCR was performed using the RNAqueous Kit, Verso One-Step RT-qPCR Kit, and SYBR Green and Low ROX mixes (Thermo Fisher) with CFX Connect Real-Time System (Bio-Rad) according to the manufacturer's protocol. The melting curves were evaluated for the samples. The target gene expressions were normalized to housekeeping gene (GAPDH) expression levels. The primers designed were: BMP-7 (forward, 5′-TACATGGGAAAC CTGGGTAAAG-3′; reverse, 5′-GGTGACATTCTGT CGGGTAAA-3′), osteocalcin (forward, 5′-TGTGTCCTCCTGGTTCATTTC-3′; reverse, 5′-CTGTCTCCCTCATGTGTTGTC-3′), and GAPDH (forward, 5′-CGCCCTGATCTGAGGTTAAAT-3′; reverse, 5′-CGGAGCAACA-GATGTGTGTA-3′).

2.12. In vivo biocompatibility, bone regeneration, histology, and immunohistochemistry

The *in vivo* biocompatibility and cranial regeneration were studied in Sprague-Dawley (SD) rats from the Capital Medical University (Beijing, China). The oxygen-generating scaffolds and the controls were implanted in SD rats which were within 280–300 g in weight each. These animal experiments were approved by the Institutional Animal Care and Use Committee (IACUC) of Xuanwu Hospital at Capital Medical (Protocol No. XWH 2019003). The *in vivo* studies included n = 3 rat subjects per group condition. A total of three group conditions were examined at 6 weeks and 12 weeks. The subjects in the blank group did not receive any scaffold implantation. The other group included subjects which received pristine GelMA without reinforcement of the oxygen-generating microparticles.

Furthermore, we have confirmed the sample size based on the resource equation approach. The degree of freedom (DF) was 12 and we used one-way ANOVA in our study.

$$DF = k(n - 1).$$

where k = number of groups and n = number of subjects per group.

We have 6 groups (blank i.e. no implant: 6 weeks, blank 12 weeks, pristine gel 6 weeks, pristine gel 12 weeks, oxygen generating gel 6 weeks and oxygen generating gel 12 weeks) and 3 samples per group. Therefore k = 6 and n = 3

$$DF = 6(3-1) = 12$$

Lastly, the oxygen-generating gel included subjects that received oxygen-generating scaffold to seal the surgical site. The DF for the error term in a one-way ANOVA in this study is in the accepted range which was reported as 10–20 by literature references [34–41]. The sample size of n = 3 was based on the previously published literature references [42–49]. These examples have previously established that the number replicates were sufficient. For statistical analyses, this sample size was based on the resource equation approach using a degree of freedom (DF) of 12 and one-way ANOVA.

For the implantation, the scaffolds were sterilized with 1% (v/v) penicillin streptomycin for 24 h prior to surgery. The animal subjects were anesthetized using 2.5% isoflurane and hypodermically injected with buprenorphine (0.05 mg/kg) pre-operatively, and then as needed. Blink response and toe pinch tests were applied to confirm the anesthetization. The heads of rats were shaved and disinfected prior to a midsagittal incision in the scalp and the pericranium removal by blunt scraping. A critical size (1 cm in diameter) round defect was created on the calvaria using a milling tool. Following, either the oxygen-generating scaffold (OGM_{60}) or the control scaffold (pristine GelMA) was inserted into the surgical site. In addition, blank control experiments were also performed in which no scaffolds filled critical defect site. The animal subjects were allowed to fully recover post-surgery. After 6 and 12 weeks, the rats were sacrificed by CO_2 inhalation. Using micro-CT, the bone regeneration within the critical size defect site was evaluated. The 3D images were reconstructed using the MIMICS 3.0 software to quantify the bone volume and bone density in the cranial injury site. The bone samples were explanted after 6 and 12 weeks and fixed in 10% paraformaldehyde overnight. The fixed samples were decalcification using 10% EDTA for 7 days at 4 °C. Subsequently, these samples were cryosection to 10 μm. The decalcified samples were stained with Hematoxylin and Eosin (H&E) to evaluate histological changes in the critical sized defect after 6 and 12 weeks. Furthermore, immunostaining for osteocalcin (OCN) was used to observed OCN protein secretion by the osteoblasts during bone regeneration. Likewise, the demonstration on bone remodeling was assessed through tartrate-resistant acidic phosphatase (TRAP) and vascular endothelial growth factor (VEGF) using this immunostaining method. The tissue sections were baked at 72 °C for 30 min. Dewaxing of the sections was performed by incubating them in xylene thrice for 10 min in containers. Subsequently, these samples were submerged in absolute ethanol, 95% ethanol, and 75% ethanol to create a gradient consecutively for 2 min in each container. Following, the samples were treated in ethylenediaminetetraacetic acid (EDTA) solution pH 9.0, and boiled in a pressurized chamber for 2.5 min. The samples slides were removed and rinsed with distilled water after cooling to room temperature. Then, the samples incubated in a 3% (v/v) solution of hydrogen peroxide in distilled water for 15 min to block the endogenous peroxidase. Afterwards, the samples were washed with PBS three times for 2 min before adding the secondary antibody dropwise to the samples. The samples incubated with the secondary antibody at 37 °C for 20 min. Again, samples were washed with PBS again three times for 2 min per wash. The samples were then stained with 3,3′-Diaminobenzidine (DAB)

solution. The DAB chromogenic solution was prepared according to the manufacturer's instructions and was added dropwise onto the tissue slices to control the coloring under the microscope and washed with once optimum tissue coloring was achieved. The samples were then rinsed thoroughly with tap water, and counterstained with hematoxylin for 2 min. Next, the samples were differentiated with 1% hydrochloric acid and absolute ethanol and rinsed with tap water which allowed their color to return to blue. The ethanol gradients were used in a reversed order to generate a dehydration gradient in the samples which were subsequently mounted on slides for imaging.

2.13. Statistical analysis

GraphPad Prism 6.0 (La Jolla, CA, USA) was used for the statistical analyses. The results were assessed by performing a one-way ANOVA. Bonferroni post hoc tests were carried out to analyze the statistically significant differences. A p-value < 0.05 was considered to be a statistically significant difference in all shown analyses. All values are represented as averages ± standard deviation (*p < 0.05, **p < 0.01, ***p < 0.001, and ****p < 0.0001).

3. Results

3.1. Characterization of the oxygen-generating scaffolds

The swelling, degradation, mechanical, and morphological behaviors were robustly characterized to assess the repertoire of physiochemical features of the oxygen-generating scaffolds. Fig. 1 shows the biomaterial properties and morphology of the synthesized CaO_2-PCL microparticles. The average size of these microparticles was 100 μm, and SEM imaging captured the topography of the microparticles when integrated within a hydrogel matrix (Fig. 1a–c). These microparticles were encapsulated within the hydrogel matrix to fabricate the oxygen-generating scaffolds. The swelling ratios shown (Fig. 1d) demonstrated a decreasing trend with the increasing concentrations of CaO_2 in microparticles. Specifically, the results show that the swelling ratios were 25%, 21%, 20%, 17%, and 11% for the pristine GelMA, OGM_0, OGM_{30}, OGM_{60}, and OGM_{90} scaffolds, respectively. Conversely, the degradation behavior showed the increasing percent mass remaining after 48 h. There were 1%, 10%, 36%, 45%, and 60% of the scaffold (%) mass remaining corresponding to the pristine GelMA, OGM_0, OGM_{30}, OGM_{60}, and OGM_{90} groups, respectively (Fig. 1e). Likewise, the mechanical properties evaluated compression tests also established a relationship between material strength and composition. The compressive moduli were 5 ± 0.81 kPa, 7 ± 0.77 kPa, 11 ± 0.8 kPa, 20 ± 0.69 kPa, and 34 ± 0.9 kPa for pristine GelMA, OGM_0, OGM_{30}, OGM_{60}, and OGM_{90} scaffolds, respectively (Fig. 1f). Therefore, the scaffolds generated distinct properties that were associated with their material compositions.

3.2. Oxygen-release kinetics

The effects of scaffold composition on the oxygen release kinetics were studied with and without microencapsulated preosteoblasts in the presence of 1 mg/mL catalase supplemented media (Fig. 2). These experiments indicated distinguishable oxygen release profiles by scaffold composition and presence of microencapsulated cells. In absence of cells, the maximum oxygen release of 29%, 30%, and 40% dissolved oxygen were achieved by day 14 for the OGM_{30}, OGM_{60}, and OGM_{90} scaffolds respectively. In contrast, the pristine GelMA and OGM_0 had no oxygen release and showed peak dissolved oxygen levels at day 0 which were 8% and 7%, respectively. These scaffolds did not contain the oxygen-generating component. The scaffolds with 3D-encapsulated preosteoblasts demonstrated oxygen release rates similar to the scaffolds without cells. For instance, the amount of oxygen was at its highest concentration on day 0 for pristine GelMA and OGM_0. There was significant reduction in oxygen concentration on day 14, indicating 3% and 2% dissolved oxygen for Pristine GelMA and OGM_0, respectively due to not having the oxygen-generating component. There was significant increase in oxygen content in the OGM_{30}, OGM_{60}, and OGM_{90} scaffolds with 25%, 28%, and 37% dissolved oxygen, respectively by day 14.

The results of the *in vitro* oxygen release kinetics show that scaffolds cultured under hypoxia without cells demonstrated significant differences between the OGM_{30}, OGM_{60}, and OGM_{90} scaffolds at the same time points (Fig. 2a). Furthermore, there was also significant difference

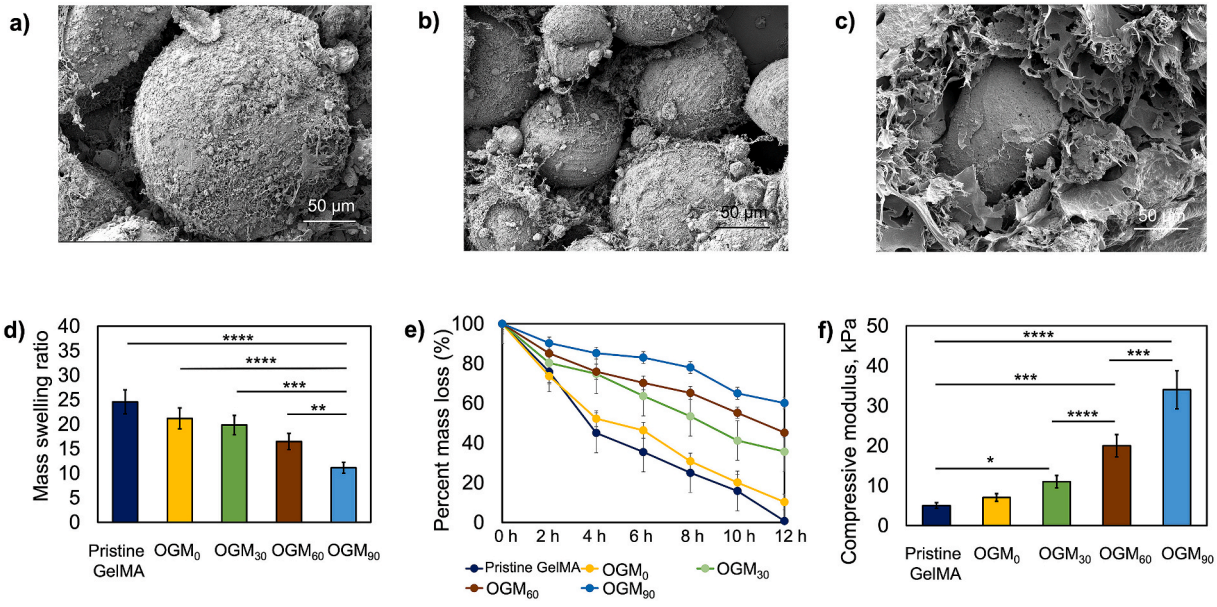

Fig. 1. Synthesis and characterization of oxygen-generating scaffolds. a-c) Scanning electron microscopy (SEM) images of the oxygen-generation scaffolds OGM_{60} show the porous microstructure, d) Swelling ratios of the pristine GelMA, OGM_0, OGM_{30}, OGM_{60}, and OGM_{90} scaffolds decreased based on the CaO_2 content in PCL, e) Degradation analysis of the oxygen-generating scaffolds via enzymatic degradation showed that the percent mass loss in the samples decreased with increasing concentrations of CaO_2, and f) Dynamic mechanical analysis (DMA) for the measurement of the compressive moduli of the oxygen-generating scaffolds. The compressive moduli increased proportional to the increasing amounts of CaO_2.

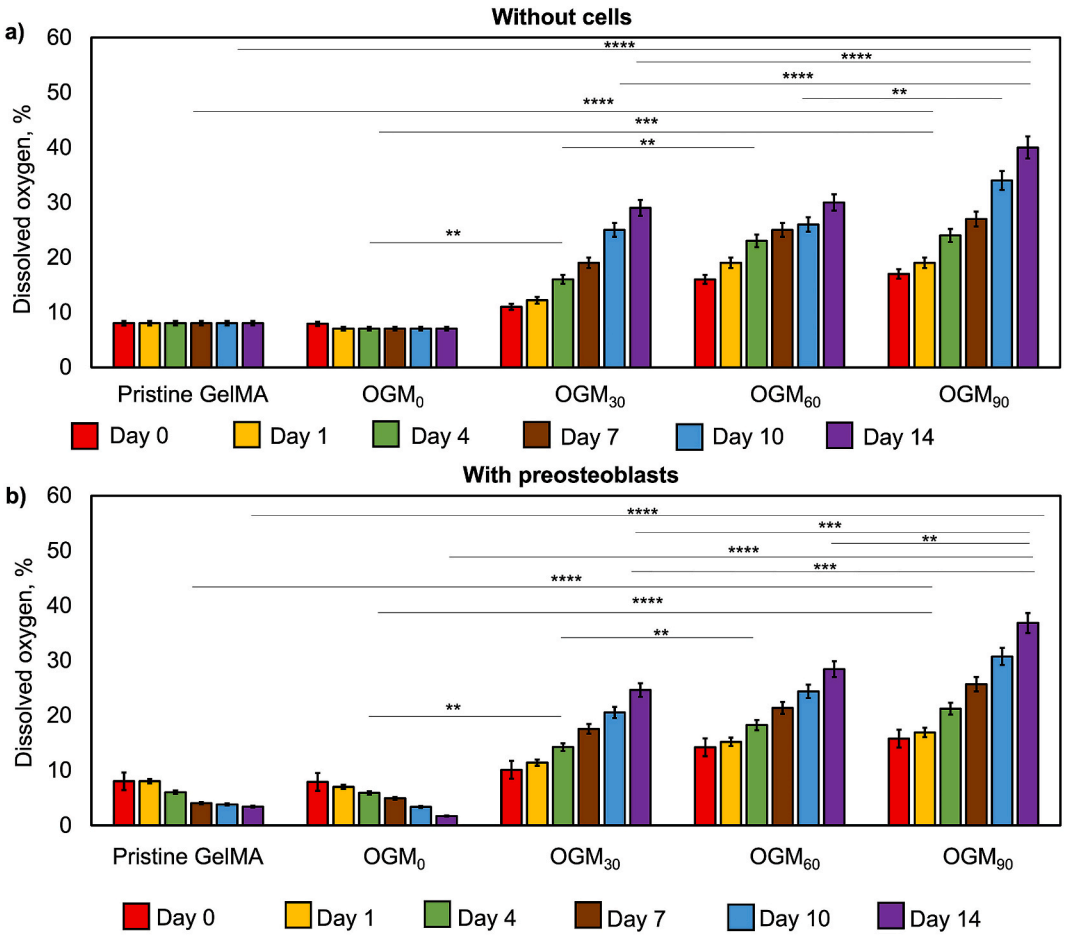

Fig. 2. Measurement of *in vitro* oxygen release kinetics of the pristine GelMA, OGM_0, OGM_{30}, OGM_{60}, and OGM_{90} scaffolds cultured under hypoxia a) without preosteoblasts and b) with 3D-encapsulated preosteoblasts. Percent oxygen availability was higher in the scaffolds that did not contain cells compared to the ones that encapsulated cells due to the oxygen consumption by the cells, as expected. The percent dissolved oxygen levels increased directly proportional to the amount of CaO_2. A p-value < 0.05 was considered to be a statistically significant difference in all shown analyses. All values are represented as averages ± standard deviation (*$p < 0.05$, **$p < 0.01$, ***$p < 0.001$, and ****$p < 0.0001$).

found each of these three groups at the same time points with respect to the pristine GelMA and OGM_0 scaffolds controls (Fig. 2a). Additionally, a similar trend was observed for the scaffolds cultured under hypoxia with 3D-encapsualted preosteoblasts. In particular, in these scaffold groups, there was significant increasing of oxygen-release as shown on days 4, 10, and 14 respectively (Fig. 2b).

3.3. Metabolic activity, alkaline phosphatase (ALP) activity, cytotoxicity, apoptosis, pH measurements and osteogenic differentiation

3.3.1. Metabolic activity of presoteoblasts in oxygen-generating scaffolds

The metabolic activity of the preosteoblasts encapsulated in the oxygen-generating scaffolds improved with increasing calcium peroxide loading over 14 days (Fig. 3a). The pristine GelMA and OGM_0 scaffolds presented the least metabolically active tissue microenvironment. The maximum metabolic activity was demonstrated by day 7 before declining for the remainder of the cell culture period. The OGM_{30} scaffolds showed comparable metabolic activity up to day 14 with respect to the control scaffolds. Interestingly, the OGM_{60} group represented the most metabolically active condition on days 0, 1, 4, 5, 10 and 14, with respect to the other conditions. While OGM_{90} scaffolds demonstrate superior metabolic activity at some of the time points, there was ultimately a decreasing trend in metabolic activity by day 14. Based on the results, there was a concentration range between 30 mg/mL to 60 mg/mL in calcium peroxide loading that supported high metabolic activity for 14 days *in vitro*.

3.3.2. ALP activity of preosteoblasts in oxygen-generating scaffolds

As described, the alkaline phosphatase (ALP) is an early marker to evaluate osteogenic differentiation [13,50]. The ALP activity of the 3D-encapsulated preosteoblasts revealed osteoinductive properties of the oxygen-generating scaffolds (Fig. 3b). The ALP activity of the preosteoblasts increased by day 14 in the oxygen-generating scaffolds; however, particularly higher ALP activity is shown in the OGM_{30} and OGM_{60} scaffolds than in the pristine GelMA and OGM_0 groups. Unlike metabolic activity, the OGM_{90} scaffolds showed the lowest ALP activity with respect to the other oxygen-generating scaffolds. At high CaO_2 loading, the OGM_{90} appeared to blunt early osteogenic differentiation. In contrast, OGM_{60} scaffolds provided maximized ALP activity within the tissue construct and exhibited the strongest osteoinductive behavior. These results were achieved without any osteogenic supplements in the media, indicating osteoinductivity of the tissue construct.

3.3.3. LDH activity of preosteoblasts in oxygen-generating scaffolds

The LDH activities of the 3D-encapsulated preosteoblasts assessed whether the oxygen-generating scaffolds demonstrated cytotoxic effects (Fig. 4a). LDH is an enzyme found in living cells and facilitates the conversion of lactate to pyruvate and the reverse reaction. LDH is released during cellular damage, and was therefore, used as a biomarker for cytotoxicity [51]. In some scaffold compositions, the LDH activity showed an increasing trend over the 14-day cell culture period. However, this trend was significantly lower and gradual in the OGM_{30} with respect to the pristine GelMA and OGM_0 scaffolds. In contrast, the

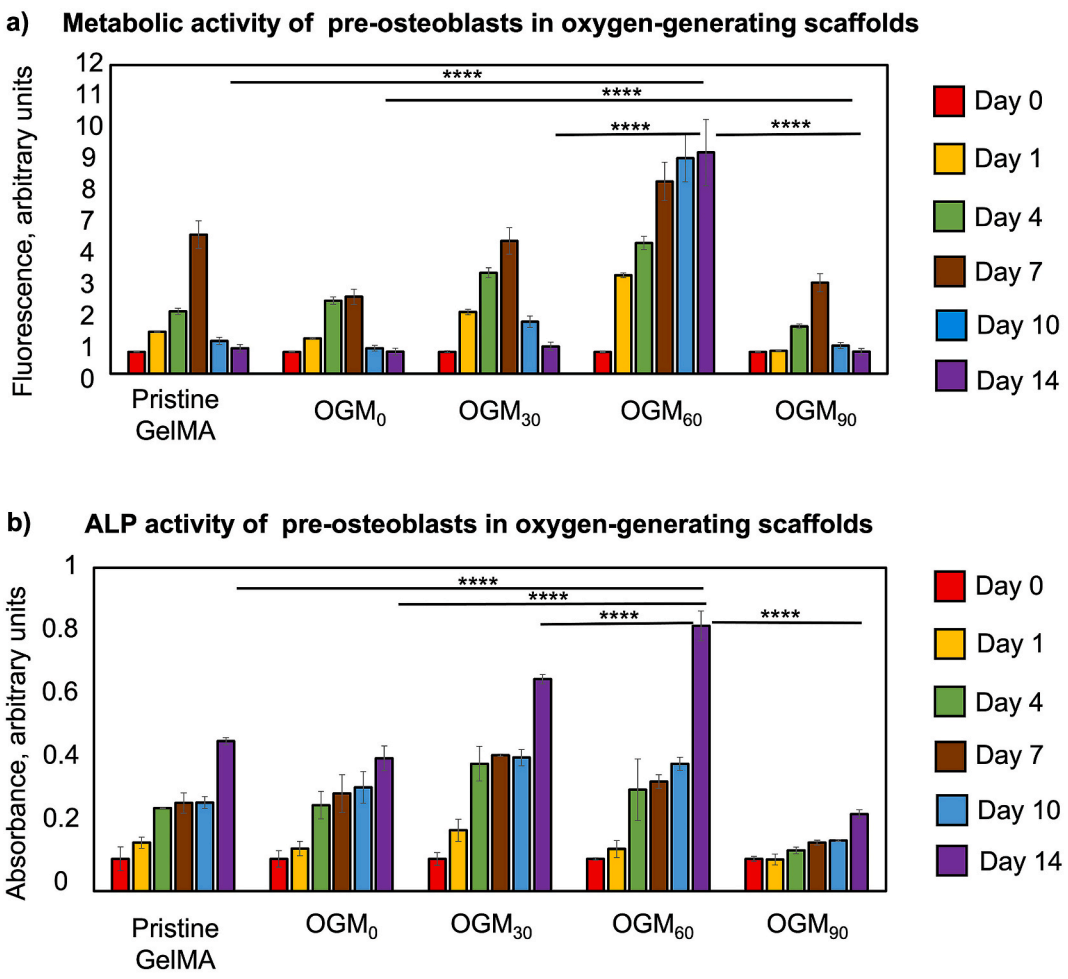

Fig. 3. Evaluation of cellular responses of encapsulated preosteoblasts to the oxygen-generating scaffolds. a) Metabolic activity of preosteoblasts, which were 3D encapsulated in the oxygen-generating scaffolds, was determined using the Alamar Blue assay. The highest metabolic activity was obtained in the OGM_{60} scaffolds and lowest one was found in the pristine GelMA group under hypoxia. b) Alkaline phosphatase (ALP) activity of the 3D encapsulated preosteoblasts was determined using an ALP assay. The OGM_{60} scaffolds showed the highest ALP activity on day 14. (*p-value <0.05 was considered statistically insignificant).

OGM_{60} scaffolds presented no significant increase in the LDH activity during the 14-day tissue culture period. Furthermore, the OGM_{60} scaffolds demonstrated the lowest LDH activity among the scaffold compositions assessed. In contrast, the OGM_{90} scaffolds showed a significant increase in the LDH activity during the 14-day in cell culture, an indication of potential cellular damage. These results are substantiated with the previous trends in metabolic and ALP activity assays.

3.3.4. *Caspase Glo 3/7 activity of preosteoblasts in oxygen-generating scaffolds*

Apoptotic activity of the tissue scaffolds was assessed through the Caspase Glo 3/7 assay (Fig. 4b). In this assay, the caspase cleaved the caspase-3/7 DEVD-aminoluciferin substrate which resulted in the release of aminoluciferin. Subsequently, the aminoluciferfin was consumed by luciferase and produced luminescence signal through the protein-protein interaction [52]. This luminescence signal was proportional to the caspase 3/7 activity, which was indicative of cellular apoptosis. The results demonstrated a significant increase in caspase 3/7 activity in the pristine GelMA and OGM_0 scaffolds. Contrarily, a lower increase in caspase 3/7 activity was observed for the cells that were cultured in the OGM_{30} scaffolds in comparison to that of the pristine GelMA and OGM_0 scaffolds. The OGM_{90} group showed the highest increase in caspase 3/7 activity across all scaffold groups. As the superior condition, the cells that were cultured in the OGM_{60} scaffolds showed the least amount of increase of caspase 3/7 activity across the duration of the 14-day culture period consistent with the previous cellular analyses.

3.3.5. *pH measurements*

The effect of the oxygen-generating scaffolds on the pH of the culture media was measured using pH strips on day 14 of the *in vitro* study (Fig. 4c). Four replicates were performed for each scaffold composition. The results showed no significant changes in the pH measurements across scaffold compositions. The pH measured remained within a range of pH 8–9 across the scaffold types during 14-day cell culture period.

3.4. *Gene expression*

The mRNA was isolated from the preosteoblasts in the oxygen-generating scaffolds and analyzed by quantitative reverse transcription Polymerase Chain Raction (RT-qPCR). The two osteogenic differentiation markers of interest in this study were the osteocalcin (OCN) and bone morphogenic protein 7 (BMP 7). BMP-7 and OCN are commonly expressed during osteogenic differentiation. Fig. 5 revealed BMP-7 and OCN gene expression after the 14-day *in vitro* tissue culture. In the OGM_{60} scaffold, BMP-7 expression was significantly higher ($p < 0.001$) than the other oxygen-generating scaffolds. The OGM_{30} scaffolds demonstrated improved gene expression for osteogenic differentiation

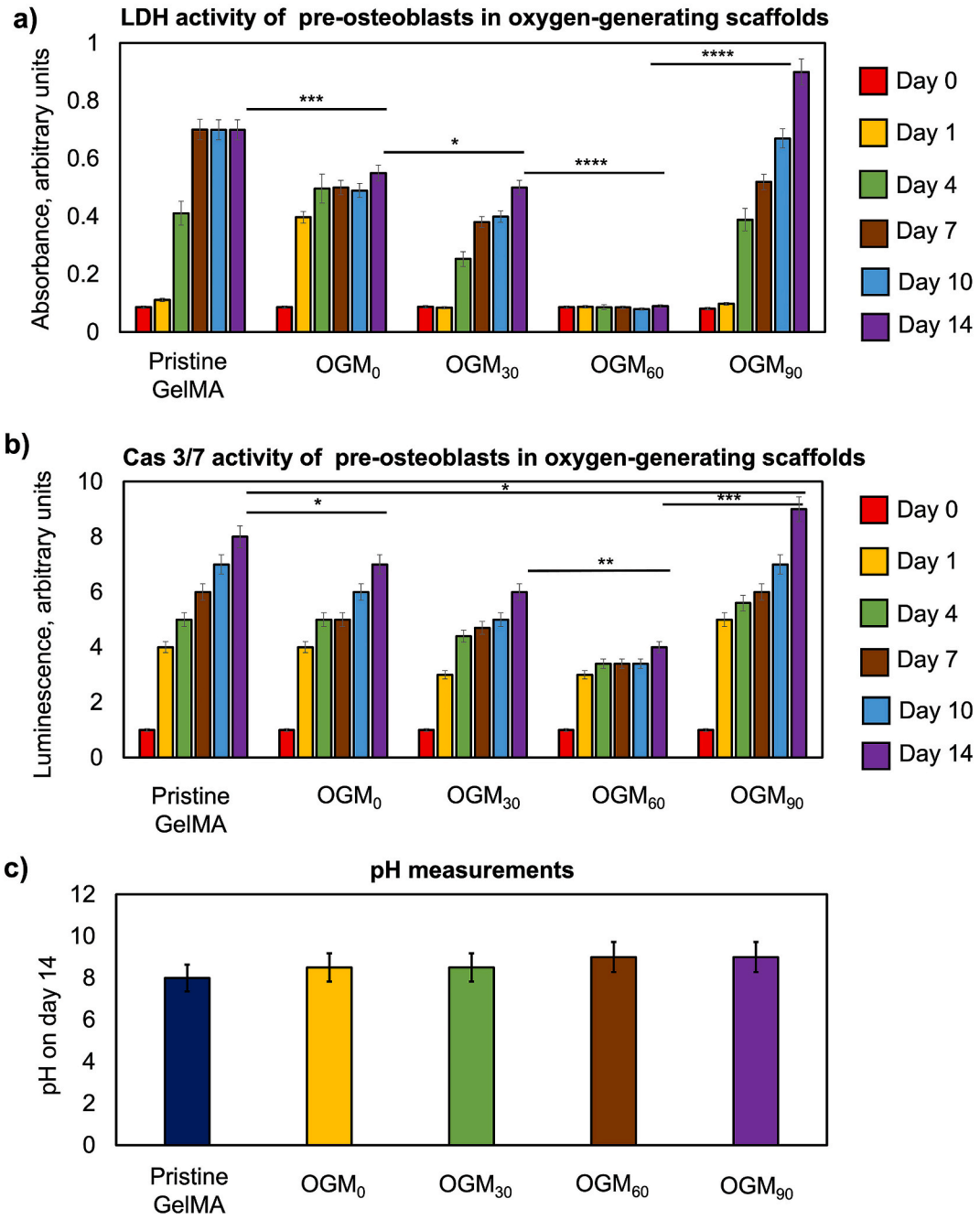

Fig. 4. Evaluation of cytotoxicity and cellular apoptosis for preosteoblasts that were cultured in the oxygen-generating scaffolds *in vitro* and pH measurements. a) LDH cytotoxicity assay was used to measure the levels of the cytosolic enzyme LDH released by the cells which have compromised plasma membrane, b) Caspase Glo 3/7 assay measured the luminescence intensity resulting from the caspase mediated cleavage of the reaction substrate that was released by the apoptotic cells, and c) The pH measurements for the oxygen-generating scaffolds were found to be similar for all experimental groups. (*p-value <0.05 was considered statistically insignificant).

with respect to the pristine GelMA and OGM_0. Interestingly, the OGM_{90} scaffolds showed low BMP-7 and OCN expression levels comparable to the pristine GelMA and the OGM_0 groups.

3.5. *In vivo* biocompatibility, bone regeneration, histology, and immunostaining

Micro-CT imaging revealed near complete bone regeneration within the critical size cranial defect at 12 weeks post-implantation (Fig. 6). At both 6 and 12 weeks, the blank control showed no bone regeneration as expected; this observation is consistent with the previous studies [53, 54]. Specifically, partial bone regeneration was achieved in pristine GelMA, with a critical gap remaining at both 6 and 12 weeks (Fig. 6d and g). While regeneration was improved with respect to the blank control, H&E staining showed that immature bone tissue was present within the hydrogel network. Moreover, the H&E staining reveal that this defect area was filled with mainly fibrous tissue in the blank at 6 and 12 weeks (Fig. 7).

As hypothesized, the optimized OGM_{60} condition facilitated almost complete bone regeneration with over 90% of the critical size cranial defect area filled. In addition, the regenerated bone volume *in vivo* was 70 mm^3 comparable to native bone (75–80 mm^3). Notably, the bone

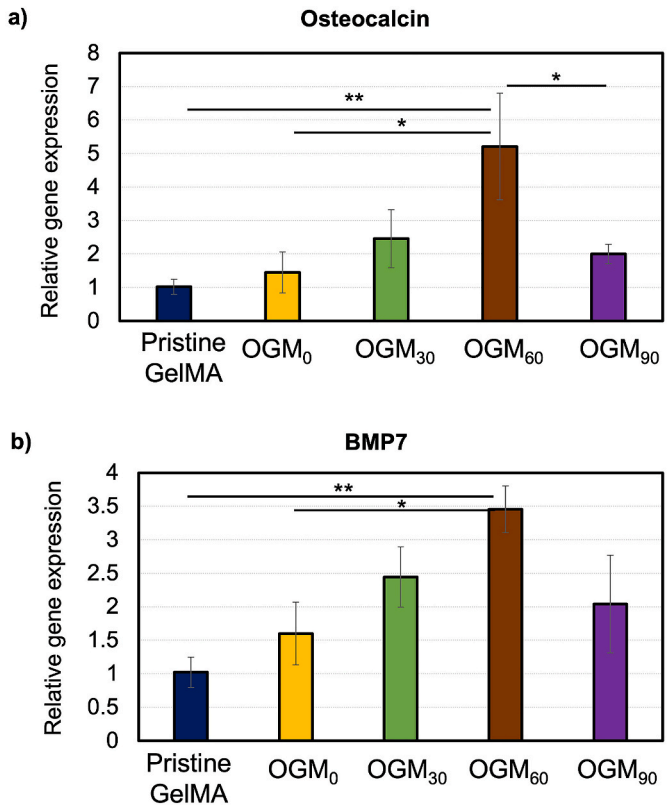

Fig. 5. Gene expression for preosteoblasts microencapsulated in oxygen-generating scaffolds. a) Osteocalcin (OCN) and b) Bone morphogenic protein-7 (BMP-7) gene expression. These genes are indicative of osteogenic differentiation. The results demonstrated that the OGM_{60} condition was the most osteoinductive scaffold group. The cells that were cultured in the OGM_{60} scaffolds provided the highest expression of OCN and BMP-7 compared to the other experimental groups. (*p-value <0.05 was considered statistically insignificant).

density was significantly higher at 12 weeks post-implantation than at 6 weeks post-implantation, showing progressive hardening of tissue (Fig. 6j and k). At 6 weeks post-implantation, the OGM_{60} group demonstrated partial maturation (50%) before the formation of predominantly cortical bone at 12 weeks. In the immunostaining results, there was significant OCN expression found in the OGM_{60} at both 6 and 12 weeks (Fig. 8). These observations corroborated with the increase in bone density which demonstrated indications of bone formation and remodeling after trauma.

3.6. Bone remodeling and vascularization of the critical size defect upon scaffold implantation

Vascularization during bone regeneration supports the recruitment of circulating osteoblast-lineage cells for ossification and bone remodeling [55,56]. Bone remodeling includes two stages, bone resorption and formation. Ultimately, the proper bone morphology and density is necessary for bone regeneration [57]. To investigate bone remodeling and vascularization within the critical sized defect area, TRAP and VEGF stainings were performed. TRAP staining in explanted tissues revealed the osteoclast activity, an indication of bone remodeling (Fig. 9) [58]. In the blank control and pristine GelMA groups, no significant tissue vascularization or osteoclast activity were present on both 6 and 12 weeks, and defects were predominantly filled with connective tissue. In the oxygen-generating OGM_{60} scaffolds, both TRAP and VEGF were present, demonstrating formation of bone tissue and osteoclast activity, respectively. The immunohistochemical results also supported that the oxygen-generating scaffolds induced significant bone regeneration within the critical sized defects. The TRAP staining confirmed the newly formed bone tissues were actively undergoing bone formation and resorption to regenerate a functional cranium. The VEGF staining showed the OGM_{60} dramatically improved vascularization with respect to the controls at 6 and 12 weeks. VEGF was also present at 6- and 12-weeks post-implantation in pristine GelMA scaffolds too. This finding suggests the porous structure of GelMA scaffold improved vascularization for tissue regeneration, as found in a previous study [59]. Overall, a comprehensive regenerative capacity was found in OGM_{60} with maximized TRAP and VEGF present during the *in vivo* study. We have shown that the oxygen-generating scaffolds induced bone regeneration to heal the critical sized cranial defects without the addition of the periosteum, bone grafts, pre-vascularization, or growth factors.

4. Discussion

4.1. Characterization of the oxygen-generating scaffolds

4.1.1. Synthesis of the oxygen-generating scaffolds and characterization of the mechanical properties

This work developed a cell culture system for the delivery and maintenance of oxygen in the extracellular microenvironment. In particular, a mean microparticle size of 100 μm was found to effectively provide sustained oxygen release with reproducible results. The standard composition of the microparticles included a 13.5% (w/v) concentration in the GelMA prepolymer matrix. In this study, a cell density of 5×10^6 cells/mL was 3D-encapsulated in the scaffolds in our system. The results suggested that oxygen generation was dependent on the amount of CaO_2 emulsified in the PCL microparticles. The other material properties that affected the oxygen release profiles included the cross-linking density, mechanical stiffness, and porosity of the scaffold. These properties inherently influence the physical behaviors of the biomaterials such as swelling, degradation, and compressive strength [27]. These physical characteristics also provided the necessary mechanical cues for cellular behaviors such as cell spreading, viability, and proliferation. The 3D matrix also dictates the permissible cell-cell interactions and the mechanotransduction which guides preosteoblast development and differentiation [60]. Other previous works have also identified hydrogel stiffness, porosity, and interconnective of pores as parameters that substantially affect cell differentiation and proliferation [21,27]. Our results showed that the microparticles progressively improved the mechanical behavior of the scaffolds with increasing CaO_2 concentrations within our scaffolds. Specifically, the CaO_2 content in the oxygen-generating microparticles was a material property that directly yielded a modular mechanical strength. Ultimately, the control and fine-tuning of the mechanical properties facilitated the osteogenic differentiation within the 3D tissue construct.

4.1.2. Swelling behavior of the oxygen-generating scaffolds

The interplay of the porosity, stiffness, and structural stability of a material affects the swelling capacity of hydrogel matrix [27,61]. The swelling properties varied as a result of the adjustments in CaO_2 concentrations within the microparticles. The findings validated that the swelling behavior was altered by modifying CaO_2 content in the scaffolds (Fig. 1d). The pristine GelMA scaffold demonstrated the most hydrophilicity as the matrix was devoid of microparticles. This increase in hydrophilicity supported a significantly high swelling ratio with respect to the microparticle-reinforced scaffolds ($p < 0.001$). The swelling behavior decreased accordingly based on the amount of CaO_2 in the microparticle reinforcement. The analysis demonstrated that the swelling behavior was correlated to the scaffold composition. For example, the OGM_{90} scaffold displayed the least swelling capacity. This swelling characteristic of the OGM_{90} scaffold was attributed to the amount of hydrophilic content. Microparticle-reinforced or composite materials generally yield a scaffold with less hydrophilic substance for

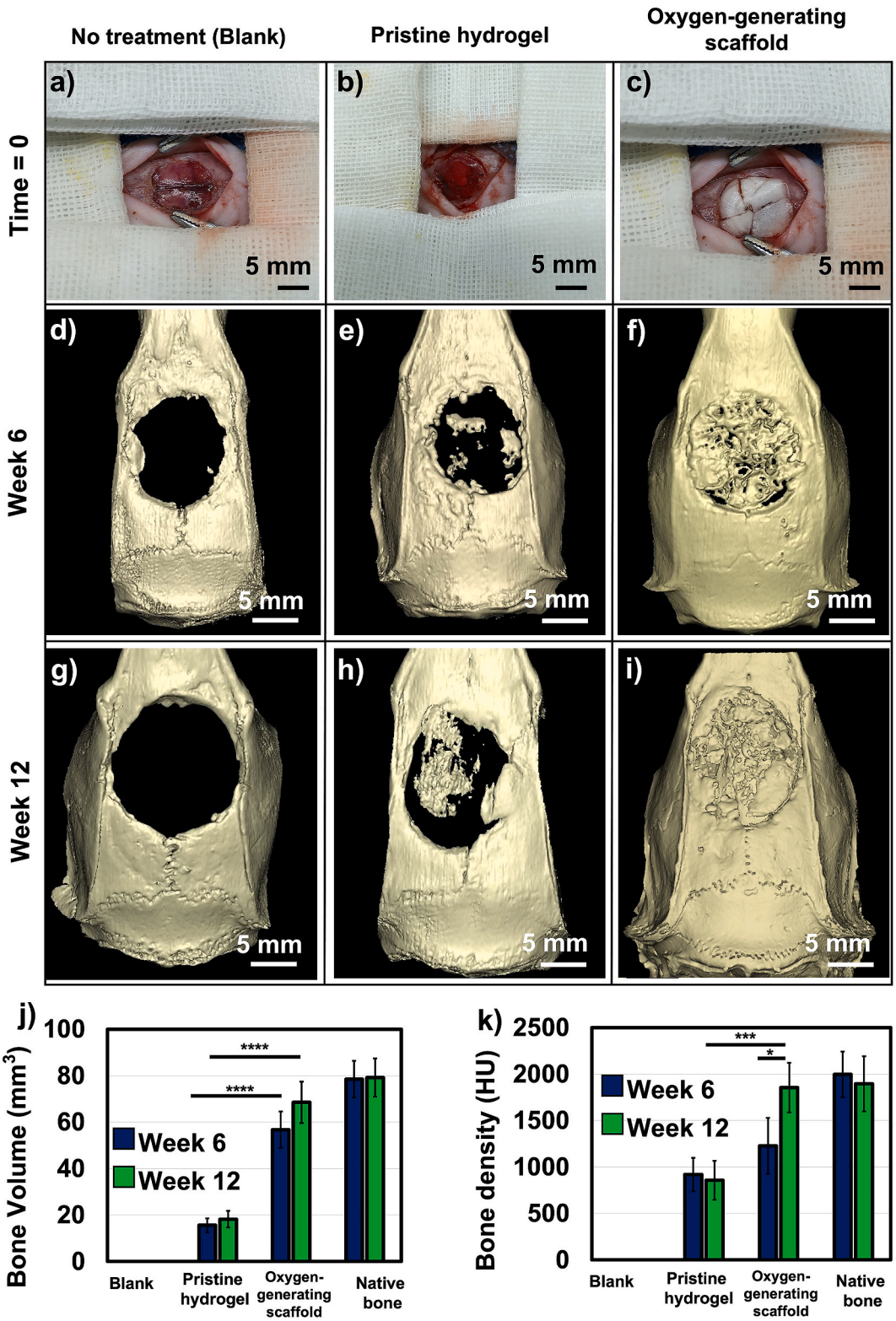

Fig. 6. Regeneration of *in vivo* critical size cranial defects in Spray Dawley (SD) rats. a) Blank control (no implant), b) Pristine GelMA scaffold, c) Oxygen-generating scaffold OGM_{60}. Bone regeneration was imaged using micro-CT on d-f) Week 6 and g-i) Week 12. The oxygen-generating scaffolds showed significantly more regeneration of the cranial defect on weeks 6 and 12. By week 12, the defect appeared to achieve near full regeneration, j) Bone volume was quantified and found to be comparable to the native bone volume for the oxygen-generating scaffolds, and k) Bone density using the oxygen-generating scaffolds was comparable to that of the native bone. (*p-value <0.05 was considered statistically insignificant).

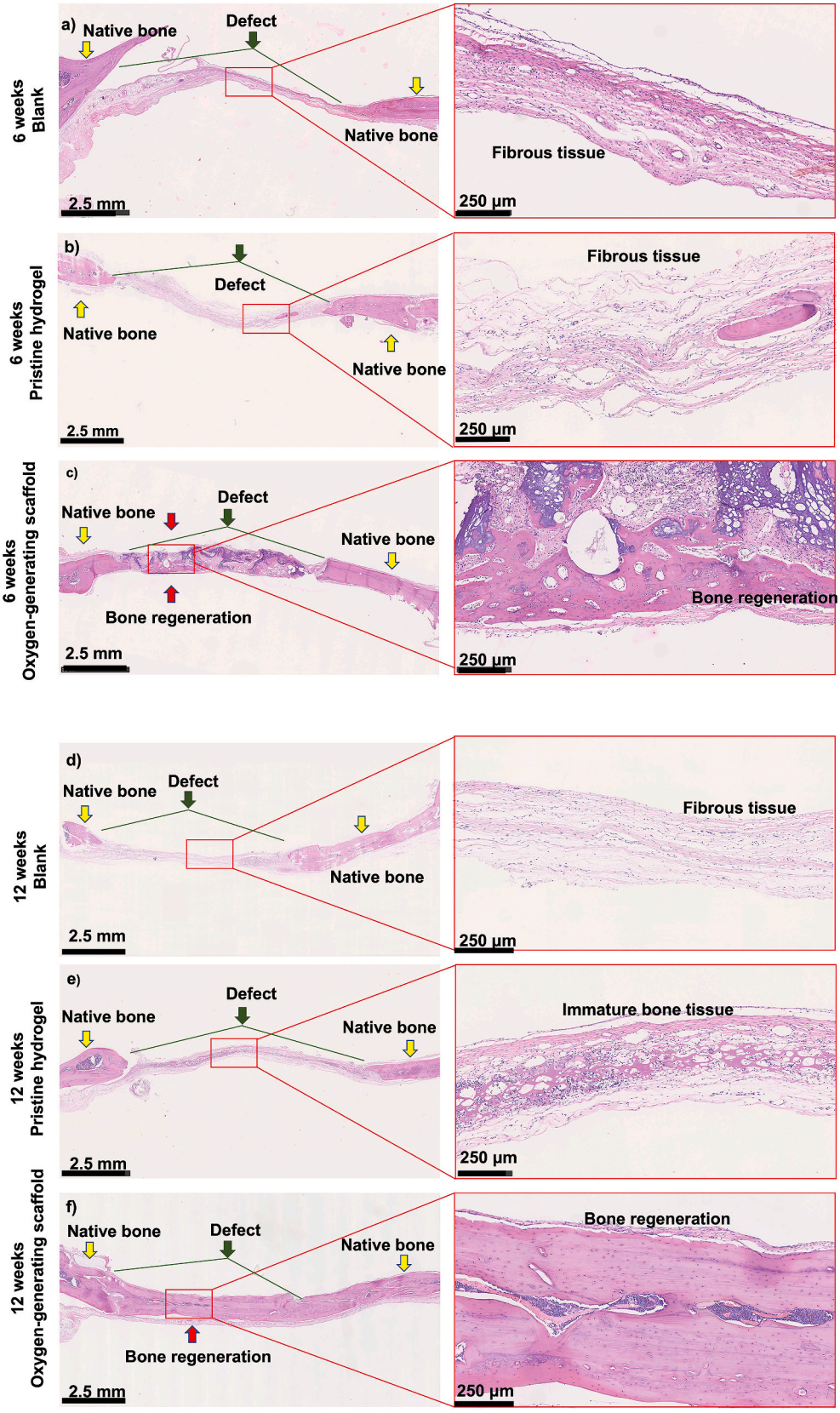

Fig. 7. Regeneration of the critical size cranial bone defect was shown by histological examination at 6 and 12 weeks. H&E staining was performed at 6 weeks for a) Blank control (no implant), b) Pristine hydrogel and c) Oxygen-generating scaffold, and at 12 weeks for d) Blank control, e) Pristine hydrogel, and f) Oxygen-generating scaffold. Images were taken at 1.25X and 10X magnification for detailed depiction. Yellow arrows indicate native bone tissue. The green arrows and lines represent the range of the original critical size bone defect. Red arrows indicate new bone formation. The results show that the oxygen-generating scaffolds support bone regeneration most effectively after 12 weeks post-op compared to the blank and the pristine hydrogel groups.

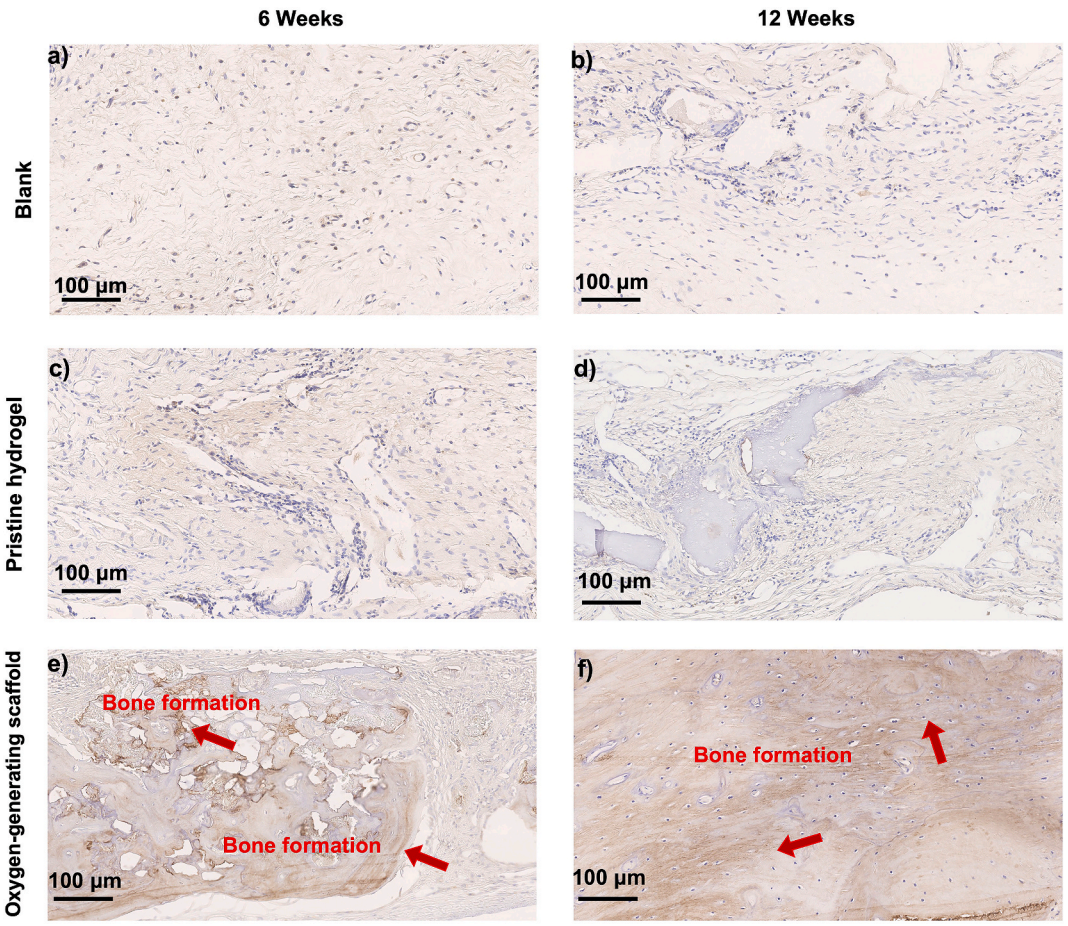

Fig. 8. Regeneration of the critical size cranial bone defect was shown by osteocalcin (OCN) staining at 6 and 12 weeks. Immunohistochemistry was performed at 6 weeks for a) Blank control, c) Pristine GelMA, and e) Oxygen-generating scaffold, and at 12 weeks for b) Blank control, d) Pristine GelMA, and f) Oxygen-generating scaffold. The arrows indicate the stained OCN in the regenerated bone tissue.

swelling [50]. Importantly in bone implants, the swelling behavior should be controlled to avoid dislodging of the tissue construct *in vivo* as the material integrates with the host tissue. The established relationship supports the control and modulation of this property through material composition with predictable results.

4.1.3. Degradation behavior of the oxygen-generating scaffolds

As the 3D scaffolds degrade, the cells encapsulated within the scaffolds deposit their extracellular matrix (ECM) into disintegrated regions of material to support tissue regeneration [62]. Ideally, the scaffold should possess degradation behavior that is similar to the rate of bone regeneration and formation. In this experiment, the degradation behavior of oxygen-generating scaffolds was determined *in vitro* via an accelerated enzymatic degradation approach (Fig. 1e). We characterized the degradation behavior using the enzyme, collagenase type II, which is natively found in the human body. The degradation behavior was indicative of potential for new tissue formation and biocompatibility for *in vivo* implantation studies. Similar to swelling behavior, the degradation rate was associated with the scaffold composition. In contrast, the increased CaO_2 within the microparticles reduced the volume of degradable material. As a result, the percent (%) mass remaining increased with scaffold reinforced with microparticles with higher CaO_2 reagent. The OGM_{90} represented the highest percent mass remaining at 48 h, indicating a slow degradation rate. This behavior was anticipated as the material was occupied with CaO_2 which is a non-degradable substance. Conversely, pristine GelMA produced the most rapid degradation rate as the material is completely degradable. The findings evidently demonstrate that manipulations of microparticle composition allows control over biodegradation which governs integration of the scaffold and generation of space for potential new tissue formation *in vitro* and *in vivo*.

4.1.4. Mechanical characterization

The mechanical competence of bone constructs is essential for mineralized tissues which undergo physiological stress and strain. The compressive moduli of the scaffolds were characterized to understand the mechanical behavior and biocompatibility of the oxygen-generating scaffolds (Fig. 1f). While PCL component remained constant in the microparticles, the CaO_2 was varied by 30 mg/mL increments. The oxygen-generating scaffolds presented distinct mechanical profiles based on the amount of CaO_2 encapsulated in the microparticles. Specifically, the compressive moduli increased with increasing CaO_2 concentrations in the microparticles. This solid moiety in the composite scaffolds supported the modularity in the mechanical strength of these tissue constructs. Therefore, the compressive moduli of these oxygen-generating scaffolds are tunable and tailorable to variety of mineralized tissues. The interface between mechanical and biological properties of bone scaffolds has implications in cell-cell communication. A broad range of rigidity of biomaterials in application would support durotaxis, a biological phenomenon that enables cell migration in response to exposure to differential architectural properties in the tissue microenvironment [63]. In turn, these mechanical properties augment the conventional bone scaffolds that often possess porosity which alone merely supports cell spreading. While the OGM scaffold presented low to moderate mechanical compressive strength *in vitro*, their use for non-load bearing *in vivo* regenerative applications show promising

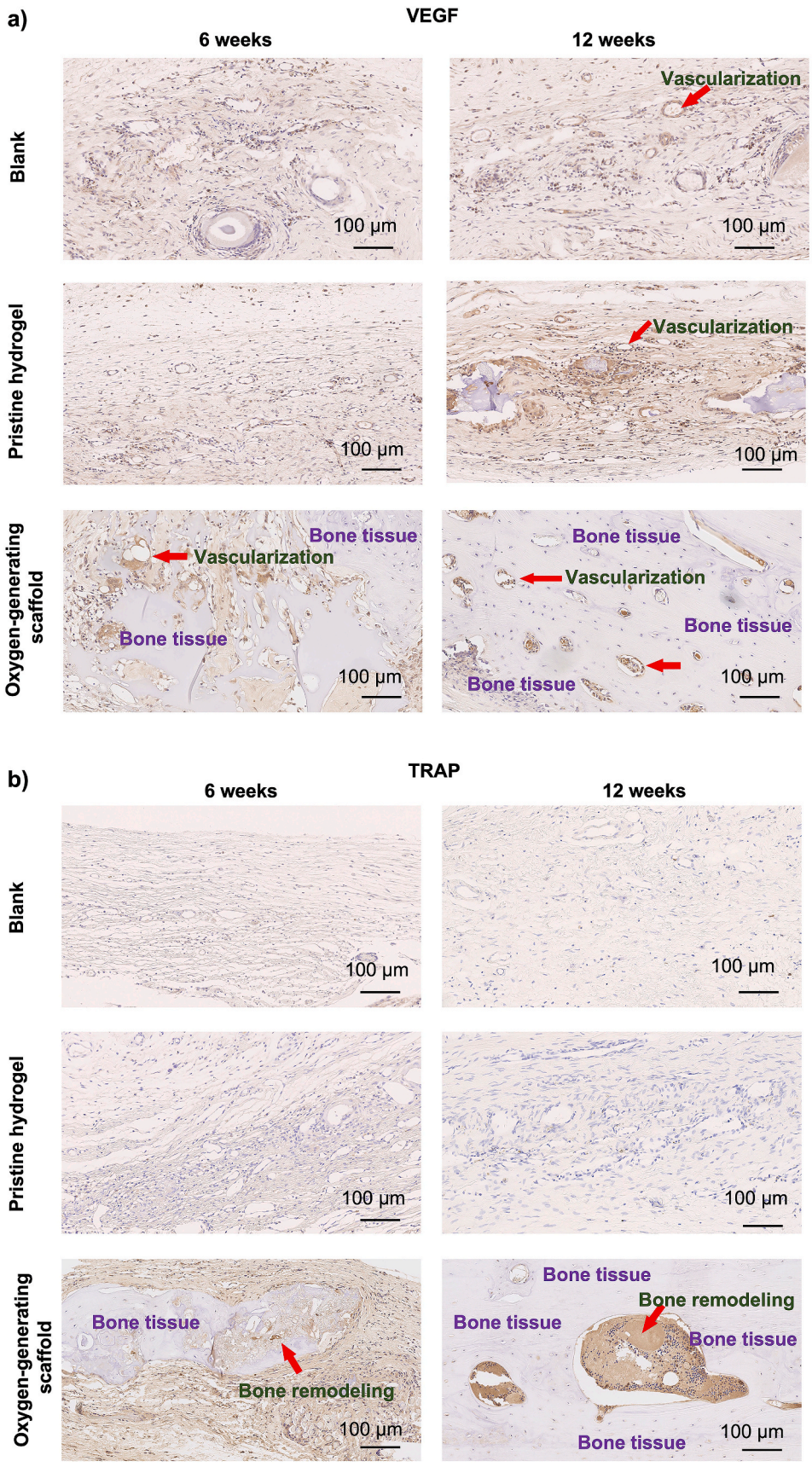

Fig. 9. Bone vascularization and remodeling of the critical bone defects were evaluated using a) Vascular endothelial growth factor (VEGF) staining and b) Tartrate-resistant acid phosphatase (TRAP) at 6 and 12 weeks of implantation *in vivo*. The results showed that the oxygen-generating scaffolds support bone remodeling and vascularization effectively compared to the blank control and pristine hydrogel groups which were devoid of the oxygen-generating reagents. The results also demonstrated that the vascularization and bone remodeling were significantly improved at the end of 12 weeks.

results in this study. Additionally, the oxygen-generating scaffolds demonstrated high tunability in terms of their physical and other mechanical properties. The mechanical analysis of the compressive strengths of the oxygen-generating scaffolds confirmed that the mechanical strength of the scaffolds can be improved by increasing the CaO_2 concentration, PCL concentration, the w/v concentration of GelMA, or the crosslinking density [29]. Furthermore, the mineralization approaches developed in this study are useful as additive to mechanically strengthen other biomaterials in *in vivo* applications [17]. Therefore, the mechanical properties of the scaffolds are modular and may be tuned according to the requirements of the specific target application. We anticipate that the mechanical properties of these scaffolds can be tuned to be mechanically competent to withstand physiological mechanical forces experienced in cranium.

4.1.5. Microarchitecture of the oxygen-generating scaffolds

The high-resolution SEM imaging for the oxygen-generating scaffolds captured microparticle morphology, distribution, pore structure, and interaction with the hydrogel matrix (Fig. 1a–c). The emulsification technique that was used to synthesize the microparticles generated microspheres that were within a 100 μm mean diameter [29]. The average diameter of the microparticles was validated by SEM imaging. The surface morphology demonstrated that these microparticles are porous and possess a rough topography (Fig. 1a–c). The cross-section image of the pristine GelMA scaffold group also revealed a highly porous interconnected matrix. The matrix morphology of the hydrogels supports cell migration and infiltration in 3D. The SEM images of the oxygen-generating scaffolds demonstrated similar characteristics and included microstructures showing microparticle-hydrogel matrix interactions. The lace-like structure covering the microparticles in particular showed integration of the microparticles within the crosslinked GelMA polymer. This microarchitecture of oxygen-generating scaffolds was a suitable 3D structure to house preosteoblasts and facilitate cell infiltration and migration.

4.2. Oxygen release kinetics

The oxygen requirement of cells in a healing tissue depends on various factors such as cell type, cell density, size of the tissue defect, scaffold porosity, degree of vascularization, tissue metabolic activity, and the diffusivity of the implanted scaffold [21]. Therefore, depending on these parameters, the oxygen requirements to heal different tissue defects will be different. Through our *in vitro* and *in vivo* experiments, we have presented the effectiveness, scalability, and adaptation of these scaffolds to an *in vivo* system. Our *in vivo* studies distinctly demonstrated significant improvement in bone regeneration and provided bone volume and density at the end of 12 weeks post-implantation with respective to native bone. The oxygen release kinetics were observed *in vitro* with and without 3D cell encapsulation. As described previously, the oxygen release kinetics were analyzed under controlled hypoxia with catalase supplemented media [21,29]. The preosteoblasts at 5×10^6 cells/mL cell seeding density were 3D encapsulated within the oxygen-generating microparticles in GelMA. The predictable oxygen release kinetics were shown in correlation to the increasing amounts of dissolved oxygen over time in scaffold compositions with higher CaO_2 loading (Fig. 2). Generally, the oxygen-generating scaffolds devoid of preosteoblasts demonstrated maximized oxygen release kinetics than scaffolds with 3D-encapsulated cells. These oxygen profiles were expected to show this behavior since the presence of preosteoblasts introduced the variable of cell oxygen consumption (Fig. 2a). The dissolved oxygen content in the pristine GelMA and the oxygen-generating scaffolds achieved a maximum oxygen release across all tissue culture conditions. After the peak release of the oxygen, the oxygen measurements plateaued briefly before decreasing gradually to day 14. As hypothesized, the oxygen release was higher in the OGM_{60} and OGM_{90} scaffolds which both contained more reagent that reacted with the water content to undergo hydrolysis. The scaffolds, such as pristine GelMA and OGM_0, which lacked CaO_2 to generate oxygen under hypoxia demonstrated negligible oxygen release over time. The 3D encapsulation of preosteoblast within these scaffolds enhanced the declining oxygen release kinetics. Therefore, the oxygen-releasing microparticles, substantially improved the amount of (%) dissolved oxygen in the cell culture systems. These oxygen-generating scaffolds were capable of supporting a stable cell culture environment for tissue construct viability for up to 14 days.

4.3. Cell proliferation, cytotoxicity, apoptosis, and ALP activity

4.3.1. Metabolic activity of the oxygen-generating hydrogels

The metabolic activities of the encapsulated preosteoblasts in the oxygen-generating scaffolds were assessed on days 1, 4, 7, 10 and 14 (Fig. 3a). The preosteoblast metabolic activities increased up to 7 days in all scaffold compositions. The OGM_{60} scaffolds represented the highest metabolic activity among the scaffolds. However, the metabolic activity was significantly lower for pristine GelMA, OGM_0, and OGM_{30} with lowest concentration of CaO_2 in PCL. The metabolic activity was compromised in the OGM_{90} condition which included the highest concentration of CaO_2 in PCL. Unlike OGM_{60}, for OGM_{90} there were declining levels of metabolic activity over time. This result indicated cellular damage possibly due to excessive oxygen in the cellular microenvironment. Furthermore, the findings suggested a favorable range of CaO_2 concentrations within PCL found in the OGM_{30} and OGM_{60} scaffolds for 3D-encapsulation. In this study, the optimal condition utilized cell seeding density of 5×10^6 cells/mL and 3D cell encapsulation in the OGM_{60} scaffold. These tissue scaffolds achieved exceptional viability and preosteoblast metabolic activity under hypoxia. The results of metabolic activity analysis revealed that there was a specific range of dissolved oxygen concentration within the cellular microenvironment that was optimal for supporting high metabolic activity upon culture for 14 days under hypoxia. Importantly, this range of required oxygen concentration is achieved through manipulation of the scaffold composition. However, it is also crucial to capture that this range is dependent on the cell type which affects oxygen consumption capacity and rates in seeding. The other confounding variables may include the cell seeding density and the scaffold dimensions. These parameters are alterable to generate scaffolds that are tunable for different applications.

4.3.2. LDH assay for evaluation of cytotoxicity

LDH is an enzyme which is released from the cells upon damage to the plasma membrane [64,65]. Therefore, LDH is indicative of cytotoxicity experienced by the cells. The LDH assay measures the LDH levels secreted by the cells encapsulated within the scaffolds into the supernatant media. LDH is an enzyme secreted by cells upon rupture of the cellular membrane which occurs during cytotoxic damage. Therefore, low LDH levels are desirable and indicative of cytocompatibility [64]. The OGM_{60} scaffolds showed no rise in LDH levels which supports that the OGM_{60} scaffolds are non-cytotoxic and do not elicit damaging cellular responses over time. This finding corroborated the bioassays which demonstrated the highest cellular metabolic activity was observed in the OGM_{60} scaffolds. The cytotoxic effects of the scaffolds to the preosteoblasts were associated to either the lack thereof or excess of oxygen release. The pristine GelMA and OGM_0 demonstrated an increased LDH activity over 14 days, suggesting increasing cytotoxicity over time (Fig. 4a). These tissue constructs in oxygen-deprived conditions were anticipated to experience hypoxia-induced cell death due to the absence of an oxygen source. The LDH assay results also were corroborated with the Alamar Blue assays which showed a deficient cell viability across 14 days in the pristine GelMA and OGM_0 groups. There was no increase in the cytotoxic effects of the OGM_{60} scaffolds which possessed the optimum CaO_2 content for oxygen-release. This experimental group showed the lowest LDH levels compared to the pristine

GelMA, OGM_0, OGM_{30} and OGM_{90} scaffolds. The OGM_{60} scaffold was therefore found to be the optimal condition with constant and stable LDH levels. Contrarily, the OGM_{90} scaffolds showed increasing LDH activity which was attributed to the cellular damage from the excess oxygen release. Therefore, the OGM_{60} scaffold composition was appropriately selected to be used in the *in vivo* studies. The low cytotoxicity observed for the OGM_{60} scaffolds coupled with the high metabolic activity confirms that the OGM_{60} scaffolds show the highest potential for biocompatibility.

4.3.3. Evaluation of apoptosis of preosteoblasts

The oxygen-generating scaffolds within optimal oxygen release potential also reduced apoptotic activity. Specifically, the oxygen release potential was defined by the amount of CaO_2 reagent encapsulated within the scaffolds. The increasing caspase 3/7 activity in the pristine GelMA and OGM_0 scaffolds were attributed to the absence of CaO_2 (Fig. 4c). In both groups, the preosteoblasts were subjected to long-term damage due to the scarcity of oxygen. The OGM_{30} scaffolds provided modest improvements to reduce apoptotic activity. The OGM_{30} scaffold improved cellular response; however, it was not sufficient for long term cytocompatibility. In contrast, the OGM_{90} scaffolds presented a considerable increase in caspase activity over time which was predictable based on the previously determined low metabolic activity and high LDH activity within this condition. The OGM_{60} scaffolds on the other hand showed constant and minimal caspase activity during *in vitro* cell culture. Based on these findings, the OGM_{60} was identified as the optimal condition for high viability of preosteoblasts and reducing apoptosis. The increase in the cellular Caspase 3/7 levels are indicative of cellular apoptosis [66]. These results indicate that by varying the CaO_2 concentration within the PCL, the biological properties of the scaffolds are tunable. We expect that altering other parameters such as PCL concentration, (w/v) ratio of the oxygen-generating microparticles in the scaffolds, GelMA concentration, cell density, and cell type would also influence the overall biological performance of the scaffolds. The *in vitro* biological analyses through cell proliferation, cytotoxicity, and cellular apoptosis support that the OGM_{60} scaffolds have the optimum scaffold composition for preosteoblast *in vitro* cell culture.

4.3.4. Alkaline phosphatase (ALP) activity of preosteoblasts in the oxygen-generating scaffolds

Alkaline phosphatase (ALP) activity levels are an indication of early osteogenic differentiation. As cells begin to differentiate, the matrix starts to mineralize causing an increase in the ALP levels [67]. Based on ALP activity assays, the oxygen-generating scaffolds elicited preosteoblast differentiation activity. These results support that the ALP activity of the encapsulated preosteoblasts increased during the 14-day tissue culture period. The ALP values of the *in vitro* cell culture study were normalized to day 0 (Fig. 3b). The maximum ALP activity was found on day 14 across all scaffolds, including pristine GelMA. However, pristine GelMA and OGM_0 demonstrated significantly lower ALP activity with respect to the other oxygen-generating scaffolds. ALP was predicted to remain at low levels as the preosteoblasts were subjected to continuous oxygen-deprived conditions. Similarly, the OGM_{90} did not demonstrate optimal ALP activity within *in vitro* tissue culture. This result can be attributed to potential cellular damage in this particular composition as indicated by the previous biological assays. The OGM_{60} scaffold supported higher ALP activity in comparison to the rest of the conditions. This behavior suggests that the presence of the oxygen-generating particles promotes early differentiation of preosteoblasts.

4.4. Osteogenic gene expression in the oxygen-generating scaffolds

The RT-qPCR analysis of the mRNA isolated from the 3D encapsulated preosteoblasts revealed the osteoinductive performance of the microparticle-reinforced scaffolds. In particular, the gene expression for BMP-7 and OCN were quantified in this study. BMP-7 and OCN are early and late osteogenic differentiation markers, respectively [13,17]. Investigation of these biomarkers was critical to discover and understand the influence of our oxygen-generating scaffolds on the osteogenic differentiation of preosteoblasts. The osteogenic gene expressions were significantly higher in the OGM_{60} scaffolds than in the other oxygen-generating scaffolds (Fig. 5). The osteogenic gene expression also increased in the OGM_{30} and OGM_{90} but was not as high compared to the OGM_{60} scaffolds. Therefore, the results suggest OGM_{60} scaffolds facilitated superior osteogenic differentiation. The other oxygen-generating scaffolds demonstrated only a modest effect on osteogenic gene expression. The OGM_{30} and OGM_{90} groups showed higher gene expression for both markers as compared to the pristine GelMA. This suggests that OGM_{30} and OGM_{90} scaffolds promoted and enhanced osteogenic gene expression to a limited degree. The results of this analysis suggest that there is a critical range of dissolved oxygen concentration in the cellular microenvironment required for these processes to occur.

4.5. Micro-CT, immunostaining, and histology in vivo

Bone regeneration within the oxygen-generating scaffolds were studied *in vivo* over 12 weeks in SD rats (Fig. 6). The OGM_{60} scaffolds were applied as the oxygen-generating scaffolds to seal and facilitate bone regeneration within round critical size cranial defects. As a control, the blank surgeries did not seal the cranial defect in order to analyze native bone regeneration. At 6 and 12 weeks, the blank control showed no bone regeneration in micro-CT imaging as expected, which was consistent with previous studies investigating regeneration of critical sized cranial defects [27,68]. In pristine GelMA, there was slight and incomplete bone regeneration at both 6 and 12 weeks post-implanted. The OGM_{60} demonstrated over a 3-fold improvement in the bone volume and bone density with respect to tissue regeneration in both the blank surgery and pristine GelMA at 6 and 12 weeks. Furthermore, the bone volume and bone density achieved are comparable to native bone at 12 weeks. Typically, porous and mechanically competent composite materials offer support for bone regeneration and connective tissue infiltration as the architectural integrity and mechanical stimuli found in bone are present [27,69]. Our composite oxygen-generating scaffolds that included a microparticle-reinforced component to deliver an oxygen supply also provided an osteoinductive substrate that favors accelerated bone regeneration. The blinded histological analyses were performed by a consulted histopathologist. These analyses were performed using similar methods that have been reported in other studies [17,70].

The osteoinductive and biomimetic features of the oxygen-generation scaffolds generated products that promoted bone regeneration. During hydrolysis of CaO_2, the reaction intermediate produces extracellular calcium ions that can facilitate mineralization around the cranial defect. The calcium ions have been shown to facilitate calcification and promote both bone formation and maturation [71,72]. The histological findings confirmed bone regeneration and tissue integration *in vivo*. The blank control revealed the presence of primarily fibrous tissue at 6 and 12 weeks, an indication of minimal bone regeneration (Fig. 7). Once the fibrous tissue occupied the defect, the bone regeneration was no longer permissible which is a behavior that has been also shown in previous literature studies [73]. The healing of bone defects would be compromised if the soft tissue occupies and heals the defect area prior to mineralization and would terminate the healing process, leading to potential nonunion defects [74]. Therefore, a tissue scaffold designed for critical bone defect should facilitate both osteogenesis and vascularization [75]. Bone regeneration within the cranium was partially present in pristine GelMA condition, demonstrating osteoblast proliferation within the hydrogel network. Based on this result, the fibrous tissue regenerated faster than the bone tissue within the cranial defect (Fig. 7). The oxygen-generating scaffold significantly improved bone formation at 6 and 12 weeks (Fig. 7c and f). The bone tissue formation was ~50%

immature at 6 weeks but showed mainly cortical bone at 12 weeks as supported by the H&E staining. This observation was further confirmed through bone density quantification results. The OCN staining was exhibited in the oxygen-generating group at both 6 and 12 weeks (Fig. 8). This evidence supports that the oxygen-generating scaffolds effectively facilitated mineralized tissue regeneration which was further confirmed through immunohistochemistry.

Specifically, the presence of TRAP and VEGF within these constructs recapitulate the required duality in bone scaffolds (Fig. 9). Essentially, the bone substitutes must promote both bone remodeling for healing critical sized defects and vascularization for integration within the host *in vivo*. The TRAP staining indicates significantly improved and continuous osteoclast activity and bone remodeling [76,77]. These activities were also evident by the presence of bone formation in the oxygen-generating scaffolds with respect to the controls. We attribute these results to the presence of the oxygen-generating component in the composite scaffolds which provided controlled and sustainable release of oxygen. The controlled oxygen release found both *in vitro* and *in vivo* is an exceptional feature of our bone substitute. In addition, the topography and mechanical strength of our scaffolds also supported the physiological cues for bone regeneration. The addition of the oxygen generating microparticles lead to physical reinforcement of the hydrogel scaffolds which also help to increase the mechanical strength of the scaffolds. The mechanical reinforcement of the scaffolds also provides cells within the defected bone with stronger substrates. This stimuli is often contribute to the induction of cell signaling pathways in bone regeneration [78]. Therefore, the development of this biomaterial addresses biomimetic features necessary for an advanced bone substitute.

VEGF notably regulates angiogenesis, and is secreted by inflammatory and stromal cells [79]. The VEGF staining showed expression both in the pristine GelMA and the oxygen-generating scaffolds possibly due to the presence of 3D hydrogel matrix for local cell attachment. Furthermore, VEGF signaling regulates the endochondral bone formation which primarily composed the new bone formation in this study [80]. Fundamentally, VEGF is quintessential in bone regeneration in critical size defects that lack the presence of the periosteum which contributes to the osteogenic properties of bone [81]. Our results validate that oxygen-generating scaffolds established favorable conditions that encouraged the initialization of bone remodeling. Bone remodeling process consists of native bone resorption and formation. This behavior determines bone morphology and density, which is necessary for proper bone regeneration [57]. The oxygen-generating scaffolds provided an optimized system for oxygen delivery in physiological conditions for maintaining long-term functional benefits. In addition to tissue viability, the oxygen-generating bone scaffold also provided a microenvironment conducive for bone formation and bone remodeling. The *in vivo* results evidently demonstrate that these scaffolds have the capacity to heal bone. The results support that these oxygen-generating scaffolds are promising tissue constructs for treatments of critical size bone defects and are compatible with other therapeutic areas that involve damaged mineralized tissues.

5. Conclusion

Oxygen supply is central to viability and function bone tissue constructs, especially of critical size. In this work, CaO_2 was emulsified in PCL to form composite oxygen-generating microparticles. These microparticles reinforced GelMA to provide sustained oxygen release over time *in vitro* and *in vivo*. Importantly, these scaffolds offered a controlled oxygen delivery system and overcame the concern of rapid hydrolysis. In this work, the encapsulated CaO_2 reacted with the water content in the hydrogel and tissue microenvironment to enable gradual release of oxygen to the tissue construct. Our *in vitro* results demonstrated that these scaffolds provide maximized cell viability, proliferation, and cytocompatibility of preosteoblasts. Moreover, this development of robust bone scaffolds demonstrated customizable biological, chemical, and mechanical properties that were adjustable through CaO_2 loading. With particular success in the OGM_{60} scaffold, these scaffolds supported various cell behaviors and differentiation *in vitro*. Furthermore, this optimized scaffold composition also achieved functional benefits while minimizing cytotoxic effects for up to 14 days in *in vitro* cell culture. The *in vivo* performance of the OGM_{60} scaffolds for regeneration of critical size cranial defects accordingly coincided with the *in vitro* findings. In particular, the micro-CT imaging revealed that the critical size defects in rat skulls regenerated >90%. The regenerated bone also possessed a bone density and bone thickness comparable to native bone. TRAP and VEGF staining of explanted scaffolds showed evidence of bone remodeling and vascularization. Our work lends itself to the broad applications of these oxygen-generating scaffolds for regeneration of defects in the mineralized tissues and engineering "off-the-shelf" bone tissue substitutes for clinical use and studying conditions that affect the bone.

Author contributions

G.C.-U. conceived the study. S.S. developed the material, and S.S. and X.W. performed the in vitro experiments. X.W, T.Z, and B.W. performed the *in vivo* experiments. G.C.-U., S.S., X.W., M.N. and A.G. wrote, revised, and edited the manuscript.

Declaration of competing interest

None.

Acknowledgements

This research was partially supported by the American Heart Association (AHA) (19TPA34910111), the University of Massachusetts Lowell faculty start-up funds, and the National Institutes of Health (NIH) (R01DE030129). The content is solely the responsibility of the authors and does not necessarily represent the official views of the National Institutes of Health. We thank Mr. Alexander Viglione for technical help.

References

[1] M.C.N. Federico C Vinas, Department of Neurological Surgery, Halifax Medical Center, Penetrating Head (Brain) Injuries (Ptbis), 2020. Medscape.
[2] T. McGrath, A. Mcgrath, R.S. Taylor, Pediatric Skull Fractures [updated 2020 apr 14], StatPearls Publishing, Treasure Island (FL), 2020.
[3] W. Wang, K.W.K. Yeung, Bone grafts and biomaterials substitutes for bone defect repair: a review, Bioactive Mater 2 (4) (2017) 224–247, https://doi.org/10.1016/j.bioactmat.2017.05.007.
[4] G.V. Research, Global Bone Graft and Substitutes Market Report, vol. 2021, 2020, p. 145, 2028.
[5] J. Hruby, R. Spunda, P. Mericka, M. Mlcek, O. Pecha, K. Splith, M. Schmelzle, F. Krenzien, J. Lindner, M. Spacek, I. Matia, Influence of the new standardized clinical cryopreservation/slow thawing protocol on immunogenicity of arterial allografts in rats, PLoS One 15 (3) (2020), e0230234, https://doi.org/10.1371/journal.pone.0230234.
[6] T. Winkler, F.A. Sass, G.N. Duda, K. Schmidt-Bleek, A review of biomaterials in bone defect healing, remaining shortcomings and future opportunities for bone tissue engineering: the unsolved challenge, Bone Joint Res 7 (3) (2018) 232–243, https://doi.org/10.1302/2046-3758.73.BJR-2017-0270.R1.
[7] Bone Grafts and Substitutes - Global Analysis and Market Forecasts, GlobalData, 2013.
[8] D. Lantigua, M.A. Nguyen, X. Wu, S. Suvarnapathaki, S. Kwon, W. Gavin, G. Camci-Unal, Synthesis and characterization of photocrosslinkable albumin-based hydrogels for biomedical applications, Soft Matter 16 (40) (2020) 9242–9252, https://doi.org/10.1039/D0SM00977F.
[9] J. An, H. Liao, N.W. Kucko, R.P. Herber, J.G. Wolke, J.J. van den Beucken, J. A. Jansen, S.C. Leeuwenburgh, Long-term evaluation of the degradation behavior of three apatite-forming calcium phosphate cements, J. Biomed. Mater. Res. 104 (5) (2016) 1072–1081, https://doi.org/10.1002/jbm.a.35641.
[10] P. Wang, Y. Song, M.D. Weir, J. Sun, L. Zhao, C.G. Simon, H.H. Xu, A self-setting ipsmsc-alginate-calcium phosphate paste for bone tissue engineering, Dent. Mater. 32 (2) (2016) 252–263, https://doi.org/10.1016/j.dental.2015.11.019.
[11] H.-S. Sohn, J.-K. Oh, Review of bone graft and bone substitutes with an emphasis on fracture surgeries, Biomater. Res. 23 (2019) 9, https://doi.org/10.1186/s40824-019-0157-y, 9.
[12] J. Tao, Y. Shin, R. Jayasinha, G.W. Buchko, S.D. Burton, A.C. Dohnalkova, Z. Wang, W.J. Shaw, B.J. Tarasevich, The energetic basis for hydroxyapatite mineralization

by amelogenin variants provides insights into the origin ofamelogenesis imperfecta, Proc. Natl. Acad. Sci. Unit. States Am. 116 (28) (2019) 13867–13872, https://doi.org/10.1073/pnas.1815654116.
[13] S. Suvarnapathaki, X. Wu, D. Lantigua, M.A. Nguyen, G. Camci-Unal, Hydroxyapatite-incorporated composite gels improve mechanical properties and bioactivity of bone scaffolds, Macromol. Biosci. (2020) 2000176, https://doi.org/10.1002/mabi.202000176.
[14] P.C. Cassino, L.S. Rosseti, O.I. Ayala, M.A.U. Martines, L.C. Portugual, C.G. D. Oliveira, I.S. Silva, R.D.A. Caldas, Potential of different hydroxyapatites as biomaterials in the bone remodeling, Acta Cir. Bras. 33 (9) (2018) 816–823, https://doi.org/10.1590/s0102-865020180090000010.
[15] B. Gaihre, S. Uswatta, A. Jayasuriya, Reconstruction of craniomaxillofacial bone defects using tissue-engineering strategies with injectable and non-injectable scaffolds, J. Funct. Biomater. 8 (4) (2017) 49, https://doi.org/10.3390/jfb8040049.
[16] X. Wu, S. Suvarnapathaki, K. Walsh, G. Camci-Unal, Paper as a scaffold for cell cultures: teaching an old material new tricks, MRS Commun 8 (1) (2018) 1–14, https://doi.org/10.1557/mrc.2018.8.
[17] X. Wu, T. Zhang, B. Hoff, S. Suvarnapathaki, D. Lantigua, C. McCarthy, B. Wu, G. Camci-Unal, Mineralized hydrogels induce bone regeneration in critical size cranial defects, Adv. Healthc. Mater. (2021) 2001101, https://doi.org/10.1002/adhm.202001101.
[18] A. Dudakovic, R.M. Samsonraj, C.R. Paradise, C. Galeano-Garces, M.O. Mol, D. Galeano-Garces, P. Zan, M.L. Galvan, M. Hevesi, O. Pichurin, R. Thaler, D. L. Begun, P. Kloen, M. Karperien, A.N. Larson, J.J. Westendorf, S.M. Cool, A.J. Van Wijnen, Inhibition of the epigenetic suppressor ezh2 primes osteogenic differentiation mediated by bmp2, J. Biol. Chem. 295 (23) (2020) P7877–P7893, https://doi.org/10.1074/jbc.ra119.011685.
[19] M. Fujioka-Kobayashi, B. Schaller, E. Kobayashi, M. Hernandez, Y. Zhang, R. J. Miron, Hyaluronic acid gel-based scaffolds as potential carrier for growth factors: an in vitro bioassay on its osteogenic potential, J. Clin. Med. 5 (12) (2016), https://doi.org/10.3390/jcm5120112.
[20] S. Pashneh-Tala, S. Macneil, F. Claeyssens, The tissue-engineered vascular graft—past, present, and future, Tissue Eng. B Rev. 22 (1) (2016) 68–100, https://doi.org/10.1089/ten.teb.2015.0100.
[21] S. Suvarnapathaki, X. Wu, D. Lantigua, M.A. Nguyen, G. Camci-Unal, Breathing life into engineered tissues using oxygen-releasing biomaterials, NPG Asia Mater. 11 (1) (2019) 65, https://doi.org/10.1038/s41427-019-0166-2.
[22] K.R. Thistlethwaite, K.J. Finlayson, P.D. Cooper, B. Brown, M.H. Bennett, G. Kay, M.T. O'Reilly, H.E. Edwards, The effectiveness of hyperbaric oxygen therapy for healing chronic venous leg ulcers: a randomized, double-blind, placebo-controlled trial, Wound Repair Regen. 26 (4) (2018) 324–331, https://doi.org/10.1111/wrr.12657.
[23] J. Grassmann, J. Schneppendahl, A. Hakimi, M. Herten, M. Betsch, T. Lögters, S. Thelen, M. Sager, M. Wild, J. Windolf, P. Jungbluth, M. Hakimi, Hyperbaric oxygen therapy improves angiogenesis and bone formation in critical sized diaphyseal defects. https://doi.org/10.1002/jor.22805, 2015, 33(4) 513-520.
[24] P. Kranke, M.H. Bennett, M. Martyn-St James, A. Schnabel, S.E. Debus, S. Weibel, Hyperbaric oxygen therapy for chronic wounds, Cochrane Database Syst. Rev. (6) (2015), Cd004123, https://doi.org/10.1002/14651858.CD004123.pub4.
[25] V.G. Sunkari, F. Lind, I.R. Botusan, A. Kashif, Z.J. Liu, S. Yla-Herttuala, K. Brismar, O. Velazquez, S.B. Catrina, Hyperbaric oxygen therapy activates hypoxia-inducible factor 1 (hif-1), which contributes to improved wound healing in diabetic mice, Wound Repair Regen. 23 (1) (2015) 98–103, https://doi.org/10.1111/wrr.12253.
[26] C.-C. Huang, W.-T. Chia, M.-F. Chung, K.-J. Lin, C.-W. Hsiao, C. Jin, W.-H. Lim, C.-C. Chen, H.-W. Sung, An implantable depot that can generate oxygen in situ for overcoming hypoxia-induced resistance to anticancer drugs in chemotherapy, J. Am. Chem. Soc. 138 (16) (2016) 5222–5225, https://doi.org/10.1021/jacs.6b01784.
[27] X. Wu, S. Stroll, D. Lantigua, S. Suvarnapathaki, G. Camci-Unal, Eggshell particle-reinforced hydrogels for bone tissue engineering: an unconventional approach, Biomater. Sci. 7 (2019), https://doi.org/10.1039/C9BM00230H.
[28] M. Touri, F. Moztarzadeh, N.A. Abu Osman, M.M. Dehghan, P. Brouki Milan, S. Farzad-Mohajeri, M. Mozafari, Oxygen-releasing scaffolds for accelerated bone regeneration, ACS Biomater. Sci. Eng. (2020), https://doi.org/10.1021/acsbiomaterials.9b01789.
[29] S. Suvarnapathaki, M.A. Nguyen, A.A. Goulopoulos, D. Lantigua, G. Camci-Unal, Engineering calcium peroxide based oxygen generating scaffolds for tissue survival, Biomater. Sci. 9 (7) (2021) 2519–2532, https://doi.org/10.1039/D0BM02048F.
[30] M. Gholipourmalekabadi, S. Zhao, B.S. Harrison, M. Mozafari, A.M. Seifalian, Oxygen-generating biomaterials: a new, viable paradigm for tissue engineering? Trends Biotechnol. 34 (12) (2016) 1010–1021, https://doi.org/10.1016/j.tibtech.2016.05.012.
[31] P.S. Patil, N. Fountas-Davis, H. Huang, M. Michelle Evancho-Chapman, J.A. Fulton, L.P. Shriver, N.D. Leipzig, Fluorinated methacrylamide chitosan hydrogels enhance collagen synthesis in wound healing through increased oxygen availability, Acta Biomater. (2016) 36 164–174, https://doi.org/10.1016/j.actbio.2016.03.022.
[32] H. Steg, A.T. Buizer, W. Woudstra, A.G. Veldhuizen, S.K. Bulstra, D.W. Grijpma, R. Kuijer, Control of oxygen release from peroxides using polymers, J. Mater. Sci. Mater. Med. 26 (7) (2015) 207, https://doi.org/10.1007/s10856-015-5542-z.
[33] A.C.A. Fontes, L. Sopchenski, C.A. Laurindo, R.D. Torres, K.C. Popat, P. Soares, Annealing temperature effect on tribocorrosion and biocompatibility properties of tio 2 nanotubes, J. Bio-Tribo-Corros. 6 (2020) 1–12, https://doi.org/10.1007/s40735-020-00363-w.
[34] B. Han, N. Perelman, B. Tang, F. Hall, E.C. Shors, M.E. Nimni, Collagen-targeted bmp3 fusion proteins arrayed on collagen matrices or porous ceramics impregnated with type i collagen enhance osteogenesis in a rat cranial defect model, J. Orthop. Res. 20 (4) (2002) 747–755, https://doi.org/10.1016/S0736-0266(01)00157-7.
[35] S.-H. Lee, S.-W. Kim, J.-I. Lee, H.-J. Yoon, The effect of platelet-rich fibrin on bone regeneration and angiogenesis in rabbit cranial defects, Tissue Eng. Regen. Med. 12 (5) (2015) 362–370, https://doi.org/10.1007/s13770-015-0031-5.
[36] H. Uusitalo, J. Rantakokko, M. Ahonen, T. Jämsä, J. Tuukkanen, V.-M. KäHäri, E. Vuorio, H. Aro, A metaphyseal defect model of the femur for studies of murine bone healing, Bone 28 (4) (2001) 423–429, https://doi.org/10.1016/S8756-3282(01)00406-9.
[37] M. Tarchala, V. Engel, J. Barralet, E.J. Harvey, A pilot study: alternative biomaterials in critical sized bone defect treatment, Injury 49 (3) (2018) 523–531, https://doi.org/10.1016/j.injury.2017.11.007.
[38] S. Toosi, H. Naderi-Meshkin, F. Kalalinia, H. HosseinKhani, A. Heirani-Tabasi, S. Havakhah, S. Nekooei, A.H. Jafarian, F. Rezaie, M.T. Peivandi, Bone defect healing is induced by collagen sponge/polyglycolic acid, J. Mater. Sci. Mater. Med. 30 (3) (2019) 1–10, https://doi.org/10.1007/s10856-019-6235-9.
[39] M. Iwasashi, M. Sakane, Y. Suetsugu, N. Ochiai, Bone Regeneration at Cortical Bone Defect with Unidirectional Porous Hydroxyapatite in Vivo, Key Eng. Mater. Trans Tech Publ., 2009, pp. 11–14. https://doi.org/10.4028/www.scientific.net/KEM.396-398.11.
[40] C. Bjartmar, J. Battistuta, N. Terada, E. Dupree, B.D. Trapp, N-acetylaspartate is an axon-specific marker of mature white matter in vivo: a biochemical and immunohistochemical study on the rat optic nerve, Ann. Neurol. 51 (1) (2002) 51–58, https://doi.org/10.1002/ana.10052.
[41] P. Ehrlich, B. Noble, H. Jessop, H. Stevens, J. Mosley, L. Lanyon, The effect of in vivo mechanical loading on estrogen receptor α expression in rat ulnar osteocytes, J. Bone Miner. Res. 17 (9) (2002) 1646–1655, https://doi.org/10.1359/jbmr.2002.17.9.1646.
[42] W.N. Arifin, W.M. Zahiruddin, Sample size calculation in animal studies using resource equation approach, MJMS 24 (5) (2017) 101, https://doi.org/10.21315/mjms2017.24.5.11.
[43] R. Mead, S.G. Gilmour, A. Mead, Statistical Principles for the Design of Experiments: Applications to Real Experiments, Cambridge University Press, 2012.
[44] M.F. Festing, D.G. Altman, Guidelines for the design and statistical analysis of experiments using laboratory animals, ILAR J. 43 (4) (2002) 244–258, https://doi.org/10.1093/ilar.43.4.244.
[45] M.F. Festing, Design and statistical methods in studies using animal models of development, ILAR J. 47 (1) (2006) 5–14, https://doi.org/10.1093/ilar.47.1.5.
[46] J. Charan, N. Kantharia, How to calculate sample size in animal studies? J. Pharmacol. Pharmacother. 4 (4) (2013) 303, https://doi.org/10.4103/0976-500X.119726.
[47] E. Agoro, G. Chinyere, E. Akubugwo, M. Wankasi, V. Agi, Some vitreous humour cardiorenal biochemical parameters as an indicator of acute carbon monoxide poisoning death: an animal model, Aust. J. Forensic Sci. 51 (4) (2019) 476–484, https://doi.org/10.1080/00450618.2011.610820.
[48] E. Agoro, E. Akubugwo, G. Chinyere, A. Ombor, Lipids levels in vitreous humor of rabbits after carbon monoxide poisoning death, SM J. Forensic Res. Criminol. 1 (1) (2017) 1004.
[49] R.C. Hubrecht, J. Kirkwood, The Ufaw Handbook on the Care and Management of Laboratory and Other Research Animals, John Wiley & Sons, 2010.
[50] X. Wu, S.I. Stroll, D. Lantigua, S. Suvarnapathaki, G. Camci-Unal, Eggshell particle-reinforced hydrogels for bone tissue engineering: an orthogonal approach, Biomater. Sci. 7 (7) (2019) 2675–2685, https://doi.org/10.1039/C9BM00230H.
[51] A. Adan, Y. Kiraz, Y. Baran, Cell proliferation and cytotoxicity assays, Curr. Pharmaceut. Biotechnol. 17 (14) (2016) 1213–1221, https://doi.org/10.2174/1389201017666160808160513.
[52] M. O'Brien, R. Moravec, T. Riss, Caspase-glo™ 3/7 Assay: Use Fewer Cells and Spend Less Time with This Homogeneous Assay, Luminescence vol. 200 (2003). ISSN: 1522-7235 Online ISSN: 1522-7243.
[53] Y. Yu, Y. Wang, W. Zhang, H. Wang, J. Li, L. Pan, F. Han, B. Li, Biomimetic periosteum-bone substitute composed of preosteoblast-derived matrix and hydrogel for large segmental bone defect repair, Acta Biomater. (2020) 113 317–327, https://doi.org/10.1016/j.actbio.2020.06.030.
[54] L. Deng, Y. Liu, L. Yang, J.-Z. Yi, F. Deng, L.-M. Zhang, Injectable and bioactive methylcellulose hydrogel carrying bone mesenchymal stem cells as a filler for critical-size defects with enhanced bone regeneration, Colloids Surf., B (2020) 111159, https://doi.org/10.1016/j.colsurfb.2020.111159.
[55] G.Z. Eghbali-Fatourechi, J. Lamsam, D. Fraser, D. Nagel, B.L. Riggs, S. Khosla, Circulating osteoblast-lineage cells in humans, N. Engl. J. Med. 352 (19) (2005) 1959–1966, https://doi.org/10.1056/NEJMoa044264.
[56] M.-H. Lafage-Proust, B. Roche, M. Langer, D. Cleret, A.V. Bossche, T. Olivier, L. Vico, Assessment of bone vascularization and its role in bone remodeling, BoneKEy Rep. 4 (2015) 662, https://doi.org/10.1038/bonekey.2015.29.
[57] L.J. Raggatt, N.C. Partridge, Cellular and molecular mechanisms of bone remodeling, J. Biol. Chem. 285 (33) (2010) 25103–25108, https://doi.org/10.1074/jbc.R109.041087.
[58] Y. Nemoto, K. Higuchi, O. Baba, A. Kudo, Y. Takano, Multinucleate osteoclasts in medaka as evidence of active bone remodeling, Bone 40 (2) (2007) 399–408, https://doi.org/10.1016/j.bone.2006.08.019.
[59] G. Eke, N. Mangir, N. Hasirci, S. MacNeil, V. Hasirci, Development of a uv crosslinked biodegradable hydrogel containing adipose derived stem cells to promote vascularization for skin wounds and tissue engineering, Biomaterials (2017) 129 188–198, https://doi.org/10.1016/j.biomaterials.2017.03.021.

[60] Y.R.V. Shih, K.F. Tseng, H.Y. Lai, C.H. Lin, O.K. Lee, Matrix stiffness regulation of integrin-mediated mechanotransduction during osteogenic differentiation of human mesenchymal stem cells, J. Bone Miner. Res. 26 (4) (2011) 730–738, https://doi.org/10.1002/jbmr.278.
[61] S. Suvarnapathaki, R. Ramos, S.W. Sawyer, S. McLoughlin, A. Ramos, S. Venn, P. Soman, Generation of cell-laden hydrogel microspheres using 3d printing-enabled microfluidics, J. Mater. Res. 33 (14) (2018) 2012–2018, https://doi.org/10.1557/jmr.2018.77.
[62] I. Cano Torres, Cell derived-extracellular matrix scaffolds with polylactic acid microcarriers for tissue engineering and cell therapy. http://hdl.handle.net/2117/132765, 2019.
[63] C. Matellan, E. Armando, Engineering the cellular mechanical microenvironment–from bulk mechanics to the nanoscale, J. Cell Sci. 132 (9) (2019), https://doi.org/10.1242/jcs.229013.
[64] S. Kamiloglu, G. Sari, T. Ozdal, E. Capanoglu, Guidelines for cell viability assays, Food Front. 1 (3) (2020) 332–349, https://doi.org/10.1002/fft2.44.
[65] T.-E. Hsieh, S.-J. Lin, L.-C. Chen, C.-C. Chen, P.-L. Lai, C.-C. Huang, Optimizing an injectable composite oxygen-generating system for relieving tissue hypoxia, Front. Bioeng. Biotechnol. 8 (2020) 511, https://doi.org/10.3389/fbioe.2020.00511.
[66] R. Tedja, A. Fox, A.B. Alvero, Detection of Anoikis Using Cell Viability Dye and Quantitation of Caspase Activity, Detection of Cell Death Mechanisms-Methos and Protocols, Springer, 2021, pp. 69–76, https://doi.org/10.1007/978-1-0716-1162-3_7.
[67] F.-Y. Cao, J.-X. Fan, Y. Long, X. Zeng, X.-Z. Zhang, A smart fluorescence nanoprobe for the detection of cellular alkaline phosphatase activity and early osteogenic differentiation, Nanomedicine 12 (5) (2016) 1313–1322, https://doi.org/10.1016/j.nano.2016.01.010.
[68] Y. Deng, H. Zhou, D. Zou, Q. Xie, X. Bi, P. Gu, X. Fan, The role of mir-31-modified adipose tissue-derived stem cells in repairing rat critical-sized calvarial defects, Biomaterials 34 (28) (2013) 6717–6728, https://doi.org/10.1016/j.biomaterials.2013.05.042.
[69] A.R. Amini, C.T. Laurencin, S.P. Nukavarapu, Bone tissue engineering: recent advances and challenges, Crit. Rev. Biomed. Eng. 40 (5) (2012), https://doi.org/10.1615/CritRevBiomedEng.v40.i5.10.
[70] M. Bartov, A. Gromov, M. Poponova, D. Savina, K. Nikitin, T. Grunina, V. Manskikh, O. Gra, V. Lunin, A. Karyagina, Modern approaches to studies of new osteogenic biomaterials on the model of regeneration of critical-size cranial defects in rats, Bull. Exp. Biol. Med. 162 (2) (2016) 273–276, https://doi.org/10.1007/s10517-016-3593-x.
[71] S.E. Kim, A.P. Tiwari, Three dimensional polycaprolactone/cellulose scaffold containing calcium-based particles: a new platform for bone regeneration, Carbohydr. Polym. (2020) 250 116880, https://doi.org/10.1016/j.carbpol.2020.116880.
[72] J. Jeong, J.H. Kim, J.H. Shim, N.S. Hwang, C.Y. Heo, Bioactive calcium phosphate materials and applications in bone regeneration, Biomater. Res. 23 (1) (2019) 1–11, https://doi.org/10.1186/s40824-018-0149-3.
[73] G. Wu, M. Pan, X. Wang, J. Wen, S. Cao, Z. Li, Y. Li, C. Qian, Z. Liu, W. Wu, Osteogenesis of peripheral blood mesenchymal stem cells in self assembling peptide nanofiber for healing critical size calvarial bony defect, Sci. Rep. 5 (2015) 16681, https://doi.org/10.1038/srep16681.
[74] C. Copuroglu, G.M. Calori, P.V. Giannoudis, Fracture non-union: who is at risk? Injury 44 (11) (2013) 1379–1382, https://doi.org/10.1016/j.injury.2013.08.003.
[75] R. Dimitriou, G.I. Mataliotakis, G.M. Calori, P.V. Giannoudis, The role of barrier membranes for guided bone regeneration and restoration of large bone defects: current experimental and clinical evidence, BMC Med. 10 (1) (2012) 1–24, https://doi.org/10.1186/1741-7015-10-81.
[76] S. Scaglione, P. Giannoni, P. Bianchini, M. Sandri, R. Marotta, G. Firpo, U. Valbusa, A. Tampieri, A. Diaspro, P. Bianco, Order versus disorder: in vivo bone formation within osteoconductive scaffolds, Sci. Rep. 2 (1) (2012) 1–6, https://doi.org/10.1038/srep00274.
[77] R.Z. LeGeros, Properties of osteoconductive biomaterials: calcium phosphates, Clin. Orthop. Relat. Res. 395 (2002) 81–98, https://doi.org/10.1097/00003086-200202000-00009.
[78] M. Crisp, Q. Liu, K. Roux, J. Rattner, C. Shanahan, B. Burke, P.D. Stahl, D. Hodzic, Coupling of the nucleus and cytoplasm: role of the linc complex, J. Cell Biol. 172 (1) (2006) 41–53, https://doi.org/10.1083/jcb.200509124.
[79] H.E. Broxmeyer, S. Cooper, Z. Li, L. Lu, H. Song, B. Kwon, R.E. Warren, D. B. Donner, Myeloid progenitor cell regulatory effects of vascular endothelial cell growth factor, Int. J. Hematol. 62 (4) (1995) 203–215, https://doi.org/10.1016/0925-5710(95)00412-2.
[80] H.-P. Gerber, T.H. Vu, A.M. Ryan, J. Kowalski, Z. Werb, N. Ferrara, Vegf couples hypertrophic cartilage remodeling, ossification and angiogenesis during endochondral bone formation, Nat. Med. 5 (6) (1999) 623–628, https://doi.org/10.1038/9467.
[81] L. Wu, Y. Gu, L. Liu, J. Tang, J. Mao, K. Xi, Z. Jiang, Y. Zhou, Y. Xu, L. Deng, Hierarchical micro/nanofibrous membranes of sustained releasing vegf for periosteal regeneration, Biomaterials (2020) 227 119555, https://doi.org/10.1016/j.biomaterials.2019.119555.